

1 **Developing a composite daily snow cover extent record**
2 **over the Tibetan Plateau from 1981 to 2016 using**
3 **multisource data**

4
5 Xiaona Chen ^a, Di Long ^{a*}, Shunlin Liang ^b, Lian He ^a, Chao Zeng ^a, Xiaohua Hao ^c, and Yang
6 Hong ^a

7 ^a *State Key Laboratory of Hydrosience and Engineering, Department of Hydraulic Engineering,*
8 *Tsinghua University, Beijing 100084, China* (*Correspondence to Di Long: dlong@tsinghua.edu.cn)

9 ^b *Department of Geographical Sciences, University of Maryland, College Park 20740, USA*

10 ^c *Northwest Institute of Eco-Environmental and Resources, Chinese Academy of Sciences, Lanzhou*
11 *730000, China*

12 **Abstract**

13 Snow cover condition across the Tibetan Plateau (TP) is not only a significant indicator of
14 climate change but also a vital variable in water availability because of its water storage function
15 in high-mountain regions of Southwest China and the surrounding Asian countries. Limited by
16 low spatial resolution, incomplete spatial coverage, and short time span of the current snow
17 cover products, the long-term snow cover change across the TP under the climate change
18 background remains unclear. To resolve this issue, a composite long-term gap-filled TP daily
19 5-km snow cover extent (SCE) record (TPSCE) is generated by integrating SCE from the

20 Advanced Very High-Resolution Radiometer (AVHRR) surface reflectance climate data record
21 (CDR) and several existing snow cover data sets, with the help of a decision tree snow cover
22 mapping algorithm, for the period 1981–2016. A snow discrimination process was used to
23 classify the land surface into snow (pre-TPSCE) and non-snow using AVHRR surface reflectance
24 CDR. To fill gaps caused by invalid observations and cloud contamination in pre-TPSCE, several
25 existing daily SCE products, including MOD10C1, MYD10C1, IMS, JASMES, and a passive
26 microwave snow depth data set are employed in the composition process. The daily snow
27 discrimination accuracy, tested by ground snow-depth observations during 2000–2014, shows
28 that the TPSCE captures the distribution of snow duration days ($R^2 = 0.80$, bias = 3.93 days)
29 effectively. The comparison between the TPSCE and fine-resolution snow cover maps
30 (MCD10A1-TP) indicates high comparability between the TPSCE and MCD10A1-TP. In
31 addition, cross-comparisons with changes in temperature, precipitation, and land surface albedo
32 indicate that the TPSCE is reliable in climate change studies. In summary, the TPSCE is spatially
33 complete and covers the longest period among all current snow cover products from satellite
34 observations. The TPSCE seamlessly records changes in snow cover across the TP over the past
35 36 years, thereby providing valuable snow information for climate change and hydrological
36 studies.

37 **Keywords:** Tibetan Plateau; Snow cover extent; AVHRR surface reflectance CDR; Climate
38 change

39 **1. Introduction**

40 Snow cover is a critical component of the cryosphere and climate system on both the local and
41 the global scales. As the "third pole" and "Asian water tower" with the highest mid-latitude
42 mountains and largest cryosphere extent outside the polar regions, the Tibetan Plateau (TP)
43 largely affects the regional environment and controls climatic and environmental changes in
44 China, Asia, and even the Northern Hemisphere (NH) at large (Kang et al., 2010; Larson, 2011;
45 Ma et al., 2009; Pu et al., 2008; Yao et al., 2012). Snow cover on the TP has large potential to
46 influence the regional hydrological cycle (Qian et al., 2011), affects the frequency of heat waves
47 in northern China (Wu et al., 2012), and results in anomalies in vegetation greenness onset
48 (Dong et al., 2013), the atmosphere–land interaction (Ma et al., 2009), and the East Asian
49 summer monsoon (Pu et al., 2008). Furthermore, seasonal snow cover across the TP constitutes a
50 vital source of surface water for Southwest China and the surrounding Asian countries (e.g.,
51 Pakistan, India, Nepal, Bangladesh, and Bhutan). Thus, quantifying snow cover conditions
52 across the TP is essential for meteorological, hydrological, ecological, and societal implications.

53 Satellite remote sensing has been employed to map and monitor snow cover for more than forty
54 years (Brown et al., 2010; Frei et al., 2012), because data collection by traditional field snow
55 surveying is time consuming, costly, and extremely difficult. Using data sets, such as the binary
56 daily snow cover mask derived from the Interactive Multi-sensor Snow and Ice Mapping System
57 (IMS) (Helfrich et al., 2007), the Northern Hemisphere Weekly Snow Cover and Sea Ice Extent
58 (NHSCE) (Helfrich et al., 2007; Robinson et al., 1993), the Moderate-Resolution Imaging

59 Spectroradiometer (MODIS) snow cover products (Hall et al., 1995), the Suomi National
60 Polar-orbiting Partnership (NPP) snow cover suite (Key et al., 2013), the European Space
61 Agency (ESA) Global Snow Monitoring for Climate Research (GlobSnow) (Pulliainen, 2006),
62 and snow water equivalent (SWE) products from the Advanced Microwave Scanning
63 Radiometer-Earth Observing System (AMSR-E) (Kelly et al., 2003) and GlobSnow, the
64 continental-scale snow cover anomalies are well quantified. Nevertheless, owing to complex
65 topography, heterogeneous land cover types, and scattered snow cover distributions over the TP,
66 as well as the limitations of the current snow cover data sets, the long-term snow cover condition
67 across the TP remains unclear. Among the current snow cover products, the Suomi-NPP has high
68 snow classification accuracy (> 90%) (Key et al. 2013), the MODIS snow cover products
69 provide moderate spatial resolution (500 m) and high temporal resolution (Hall et al., 1995), the
70 IMS provides complete spatial coverage (Helfrich et al., 2007), and the NHSCE provides the
71 longest time span (4 October 1966 to the present) (Helfrich et al., 2007; Robinson et al., 1993).
72 However, incomplete spatial coverage (e.g., Suomi-NPP and MODIS), short time span (e.g.,
73 Suomi-NPP and IMS), and low spatial resolution (e.g., NHSCE and GlobSnow) largely restrict
74 the application of these products in snow cover studies across the TP.

75 To improve the understanding of snow cover changes over the TP under the climate change
76 background, a long-term series, temporally consistent, and high-quality composite snow cover
77 data set is needed. Accordingly, the objective of this study was to develop a composite long-term
78 TP daily 5-km snow cover extent (SCE) record (TPSCE). To generate the preliminary daily

79 TPSCE (pre-TPSCE) at the highest achievable spatial resolution and longest time span, we
80 employed the newly published National Oceanic and Atmospheric Administration (NOAA)
81 Advanced Very High-Resolution Radiometer (AVHRR) surface reflectance Climate Data Record
82 (CDR) (Vermote et al. 2014) as primary data. To overcome the shortage of optical AVHRR
83 images in snow discrimination (mainly caused by invalid observations and cloud contamination),
84 several ancillary data sets were jointly used in this study. Moreover, to test the reliability of the
85 TPSCE in climate change studies, temperature, precipitation, and land surface albedo data were
86 employed for cross-comparison purposes.

87 This study comprises six sections. Section 2 describes the data sets used in the study. Section 3
88 presents the processing flowchart for the TPSCE. In section 4, we compare the TPSCE with
89 ground snow-depth observations and fine-resolution snow cover maps. We analyze the
90 spatiotemporal variability in SCE from the TPSCE in section 5 and present cross-comparisons
91 with temperatures, precipitation, and land surface albedo. Finally, in section 6, we summarize
92 this study and present our conclusions.

93 **2. Data sets and Methodology**

94 **2.1. Data sets**

95 **2.1.1. AVHRR surface reflectance CDR**

96 The AVHRR surface reflectance CDR is processed from the AVHRR Global Area Coverage
97 (GAC) Level 1b data set. The AVHRR GAC observations are packaged into data arrays, with
98 latitudinal and longitudinal dimensions of 3600×7200, covering the globe at 0.05° spatial

99 resolution (Vermote et al., 2014). The spectral bands of AVHRR surface reflectance CDR are
 100 summarized in Table 1. The quality control descriptions are listed in Table 2.

101 **Table 1.**

102 Details of spectral bands of AVHRR surface reflectance CDR used in this study.

Bands	Wavelength (μ m)	Description
1	0.58–0.68	surface reflectance at 640 nm (SR1)
2	0.725–1.00	surface reflectance at 860 nm (SR2)
3	3.55–3.93	surface reflectance at 3.75 microns (SR3)
4	3.55–3.93	brightness temperature at 3.75 microns (BT37)
5	10.30–11.30	brightness temperature at 11.0 microns (BT11)
6	11.50–12.50	brightness temperature at 12.0 microns (BT12)
7	-	quality control flag

103 **Table 2.**

104 Quality control descriptions of AVHRR surface reflectance CDR used in this study.

Bit	Description	Value=1	Value=0
15	polar flag (latitude over 60 degrees (land) or 50 degrees (ocean))	Yes	No
14	BRDF-correction issues	Yes	No
13	RHO3 value is invalid	Yes	No
12	Channel 5 value is invalid	Yes	No
11	Channel 4 value is invalid	Yes	No
10	Channel 3 value is invalid	Yes	No
9	Channel 2 value is invalid	Yes	No
8	Channel 1 value is invalid	Yes	No
7	Channels 1 - 5 are valid	Yes	No
6	Pixel is at night (high solar zenith)	Yes	No
5	Pixel is over dense dark vegetation	Yes	No

4	Pixel is over sunglint	Yes	No
3	Pixel is over water	Yes	No
2	Pixel contains cloud shadow	Yes	No
1	Pixel is cloudy	Yes	No

105 Compared with AVHRR data sets used in previous studies ([Hori et al., 2017](#); [Zhou et al., 2013](#)),
106 AVHRR surface reflectance CDR provides consistent daily average surface reflectance and
107 brightness temperatures that are derived from the AVHRR sensors onboard seven NOAA polar
108 orbiting satellites, including NOAA-7, NOAA-9, NOAA-11, NOAA-14, NOAA-16, NOAA-17,
109 and NOAA-18 ([Vermote et al., 2014](#)). Moreover, AVHRR surface reflectance CDR calibrates
110 different instruments from 1981 to the present and facilitates their use in current snow mapping
111 studies. Evaluating the AVHRR surface reflectance CDR performance by cross-comparison with
112 MODIS in the monitoring of United States wheat yield demonstrated that the utility errors of
113 AVHRR surface reflectance CDR were equivalent to those derived from MODIS ([Franch et al.,](#)
114 [2017](#)). Therefore, this AVHRR historical data set was found to be reliable in land cover
115 classification, especially for years before 2000. In addition, to reduce the snow discrimination
116 error caused by distortions in pixel geometry, only images with a view zenith angle of less than
117 45° were used in this study.

118 Compared with binary snow cover products, fractional snow cover products would provide better
119 accuracy because of fragmented snow distributions in the TP. However, due to complex
120 topography and relatively low spatial resolution of AVHRR surface reflectance CDR (0.05°), the
121 selection of end-members within a grid cell across the TP is variable and uncertain, which limits

122 the application of spectral unmixing algorithms among images with different times and locations.

123 Thus, we developed binary snow products instead of fractional snow cover products in this study.

124 **2.1.2. Ancillary data**

125 (1) MODIS daily snow cover products

126 The MODIS Terra/Aqua Snow Cover Daily L3 Global 0.05° Climate Modeling Grid (CMG)

127 (MO/YD10C1) (Hall et al., 1995) reports the percentage of snow-covered land at 0.05° spatial

128 resolution for the period 2000 to the present and 2002 to the present, respectively. The

129 percentages are computed from snow cover observations in the MODIS Terra/Aqua Snow Cover

130 Daily L3 Global 500-m Grid (MO/YD10A1) data set (Hall et al., 1995). The overall absolute

131 accuracy of MOD10A1 is higher than 93% under ideal conditions of illumination, clear skies,

132 and several centimeters of snow on a smooth surface (Hall and Riggs, 2007). A study by

133 Polashenski et al. (2015) indicated that Collection 5 MODIS data, particularly that of Terra,

134 showed systematic temporal trends in visible and near-infrared bands. To avoid uncertainties

135 induced by this issue in MO/YD10C1, we used collection 6 MO/YD10C1 in our study. However,

136 limited by cloud contamination, swath coverage, warm bright surface features, and low

137 illumination, the spatial coverages of MO/YD10C1 are not complete.

138 (2) IMS snow cover product

139 The IMS snow cover product is created manually by a snow analyst observing all the available

140 satellite imagery, automated snow mapping algorithms, and other ancillary data (Helfrich et al.,

141 2007). This data set provides daily snow cover maps for the NH from February 1997 to the

142 present at three different resolutions, i.e., 1 km, 4 km, and 24 km. To fill the gaps in the
143 pre-TPSCE at the highest achievable spatial resolution, we used the IMS snow mask at 4-km
144 spatial resolution from early 2004 to the present. The daily rate of agreement between the IMS
145 snow maps and ground snow observations between 2006 and 2010 ranged mostly between 80%
146 and 90% through winter seasons (Chen et al., 2012). However, the snow classification accuracy
147 of IMS is only 60% because of serious omission error over the TP as was evaluated by Yu et al.
148 (2016).

149 (3) JASMES snow cover product

150 The NH daily 5-km SCE product (JASMES) was developed by the application of a consistent
151 objective snow cover mapping algorithm to data from historical optical sensors on polar orbiting
152 satellites during 1978–2015, including AVHRR GAC radiance data of NOAA from November
153 1978 to December 2005, and MODIS radiance data (MOD02SSH of Terra, MYS02SSH of Aqua)
154 from March 2000 to December 2015 (Hori et al., 2017). Owing to gaps caused by track, swath,
155 solar zenith angle, view zenith angle, and cloud contamination, the JASMES daily SCE data are
156 not spatially complete. Comparison with NOAA weekly SCE that is corrected by in situ data
157 indicates the reliability of the long-term trends of the JASMES product. However, the correlation
158 between the annual snow duration (SCD) trends derived from both in situ measurements and
159 JASMES showed that there is not only a weak correlation between SCD trends from the
160 JASMES and in situ data ($R=0.330$ for NH) but also an overestimation tendency of the
161 JASMES-derived trends (Hori et al., 2017). Since the systematical error between AVHRR and

162 MODIS could influence the consistency of the JASMES data set, we used only the JASMES
163 generated by the NOAA AVHRR GAC radiance data in this study.

164 (4) Passive microwave snow-depth data

165 Compared with optical remote sensing, passive microwave sensors offer the potential to estimate
166 snow cover under cloudy conditions (Frei et al., 2012). To partially address the cloud
167 contamination issue that exists in optical snow cover data sets, the passive microwave derived
168 snow-depth data set (PSD) developed by Che et al. (2008) was employed in this study. The PSD
169 data set at 25-km spatial resolution was retrieved from inter-calibrated brightness temperature
170 data from the Nimbus-7 Scanning Multichannel Microwave Radiometer (SMMR) during 1978–
171 1987, the Defense Meteorological Satellite Program (DMSP) Special Sensor Microwave/Imagers
172 (SSM/I) during 1987–2007, and the DMSP Special Sensor Microwave Imager/Sounder (SSMIS)
173 during 2008–2016 by using the modified Chang algorithm and a dynamically adjusted algorithm
174 (Che et al., 2008). The inter-sensor calibration improved the consistency of the daily snow-depth
175 products and provided a temporally consistent, long-term series of snow-depth data set over
176 China, which were important in the development of the TPSCE. However, there are
177 misclassification and errors in the PSD-derived SCE due to relatively coarse spatial resolution of
178 passive microwave remote sensing, ground temperature, snow characteristics and topography
179 according to Dai et al. (2017), especially over the frozen ground (Tsutsui and Koike 2012).

180 (5) Landsat 5 TM data

181 Landsat 5 TM images at 30-m spatial resolution were employed as "ground truth" to adjust the

182 threshold of the normalized difference snow index (NDSI) applied in the snow discrimination
183 process. Since both Landsat 5 TM images and AVHRR surface reflectance CDR are often
184 contaminated by cloud cover, few images are ideal in the comparison process. After
185 cross-comparison of cloud cover from Landsat 5 TM images and AVHRR surface reflectance
186 CDR, only two Landsat 5 TM images were selected in this study. Details of the two Landsat 5
187 images are listed in Table 3.

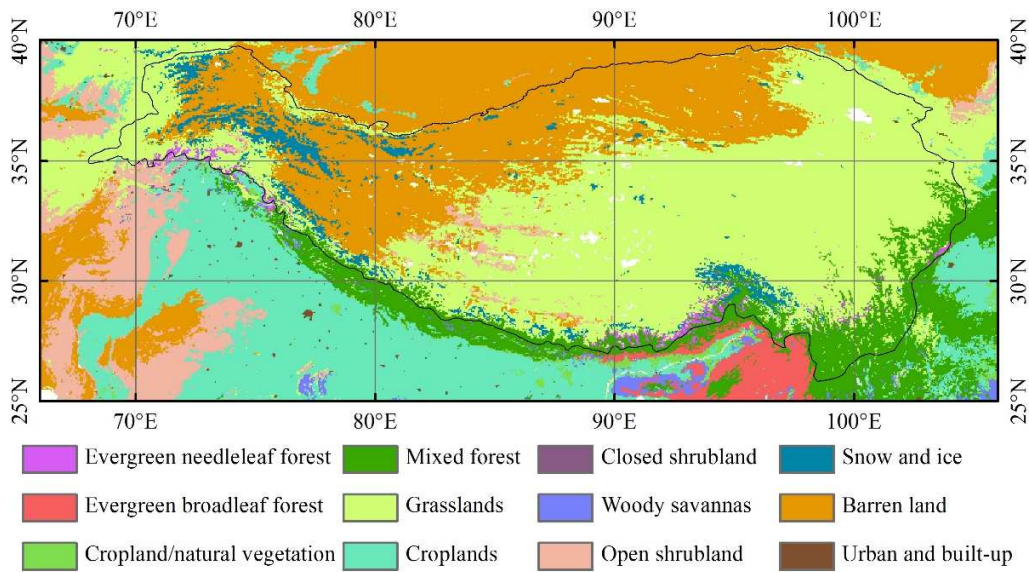
188 **Table 3.**

189 Details of Landsat images used in this study.

No.	Path	Row	Date	Cloud cover (%)	Latitude (°N)	Longitude (°N)
A	149	035	2011-04-27	2.85	75.23	36.05
B	151	035	2011-04-25	1.86	72.15	36.05

190 (6) Land cover types data

191 To increase the snow discrimination accuracy from the AVHRR surface reflectance CDR, the
192 generation of the TPSCE was initiated within the framework of the International Geosphere
193 Biosphere Program (IGBP) land cover types from MCD12Q1. The IGBP divides the land surface
194 into 17 types, including 11 natural vegetation types, 3 land use and land mosaic types, and 3
195 vegetation-free land types (Friedl et al., 2010). The land cover types over the TP derived from
196 MCD12Q1 in 2012 are presented in Fig. 1.



197

198 **Fig. 1.** Location and distribution of IGBP land cover types across the TP derived from MCD12Q1 in 2012.

199 To increase the effectiveness of discriminating snow cover from other land surfaces, we
 200 re-classified the land cover types defined by the IGBP across the TP into four types, i.e., (1)
 201 mixed forest and shrublands, (2) grasslands, (3) barren land, and (4) snow and ice. The mixed
 202 forest and shrublands, including evergreen needle-leaf forest, evergreen broad-leaf forest, mixed
 203 forest, closed shrublands, open shrublands, and woody savannas are defined by the IGBP. The
 204 grasslands, including cropland/natural vegetation, grasslands, and cropland are also defined by
 205 the IGBP. The barren land, including barren or sparsely vegetated, urban, and built-up is defined
 206 by the IGBP. The snow and ice types equal to the types defined by the IGBP.

207 (7) Elevation data

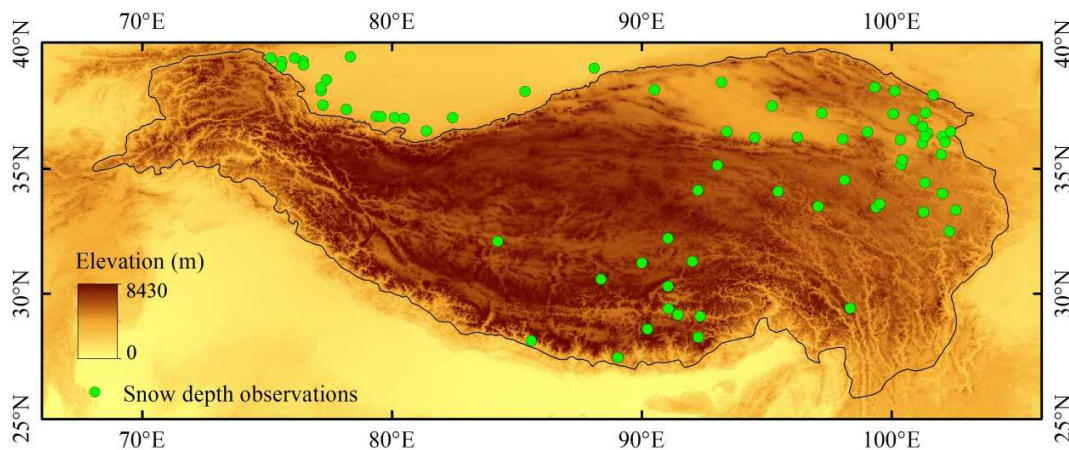
208 To detect cloud before the snow discrimination process, the digital elevation model (DEM)
 209 derived from the Shuttle Radar Topography Mission (SRTM) was used in this study. To match

210 the resolution of the AVHRR surface reflectance CDR, we resampled the original SRTM DEM
211 data at a 90-m resolution to a 0.05° spatial resolution by using a resampling method of "average"
212 with the help of gdalwarp (<http://www.gdal.org/gdalwarp.html>).

213 2.1.3 Cross-comparison data

214 (1) Ground snow-depth observations

215 The ground snow-depth observations were needed to verify the performance of the TPSCE to
216 capture the actual snow distribution across the TP. In this study, daily snow-depth observations
217 for the period 2000–2014 were employed for this purpose. The daily snow-depth observations
218 were obtained from the Data Sharing Service Platform of the China Meteorological
219 Administration (CMA, <http://data.cma.cn/>). The distribution of 72 ground snow-depth
220 observations employed in this study is shown in Fig. 2.



221 **Fig. 2.** Distribution of 72 ground snow-depth observations over the TP and surroundings for the period 2000–2014.

223 (2) MCD10A1-TP snow cover products

224 The combined fine-resolution cloud-free gap-filled MODIS daily snow cover data set across the

225 TP (MCD10A1-TP) developed by Huang et al. (2014) was used in this study to compare with the
226 climatology and anomalies of the snow cover over the TP calculated from the TPSCE.
227 MCD10A1-TP was generated by using daily MOD10A1, MYD10A1, and AMSR-E SWE
228 products. By combining optical and passive microwave snow products, the overall classification
229 accuracy of MCD10A1-TP reaches 91.7% when the snow depth is more than 3 cm (Huang et al.,
230 2014), suggesting that MCD10A1-TP is suited for use as a benchmark in our study.

231 (3) Land surface temperature data

232 To evaluate long-term snow cover changes derived from the TPSCE by cross-comparison, the
233 daily-averaged land surface temperature data set, gridded at 0.25° horizontal resolution, derived
234 from the European Centre for Medium-Range Weather Forecasts Reanalysis (ECMWF)
235 (ERA-Interim) (Dee et al., 2011) during 1981–2016, was used in this study. ERA-Interim is
236 widely employed in global and regional climate change studies, e.g., Chen et al. (2015), Cohen et
237 al. (2010), and Cohen et al. (2014). Evaluation of ERA-interim monthly temperature data over
238 the TP using 75 ground meteorological stations showed high correlations ranging from 0.97 to
239 0.99 during 1979–2010 (Gao et al., 2014).

240 (4) Precipitation data

241 Similar with the land surface temperature data, the Precipitation Estimation from Remotely
242 Sensed Information using Artificial Neural Networks-Climate Data Record (PERSIANN-CDR)
243 (Ashouri et al. 2015) was also employed to compare with long-term snow cover changes derived
244 from the TPSCE. PERSIANN precipitation CDR provides daily precipitation estimates at a

245 spatial resolution of 0.25° in latitudes from 60°S to 60°N from 1983 to the end of 2015. This
246 product was developed by using Gridded Satellite (GridSat-B1) infrared data that were derived
247 from merging International Satellite Cloud Climatology Project (ISCCP) B1 infrared data and
248 Global Precipitation Climatology Project (GPCP) version 2.2 (Ashouri et al., 2015).

249 (5) CLARA-SAL land surface albedo data

250 Changes in snow cover have been shown to be related closely with anomalies in land surface
251 albedo because of high reflectance of snow cover (Chen et al., 2015; Qu and Hall, 2014).
252 Therefore, the long-term surface albedo data set derived from CLOUD, Albedo and surface
253 Radiation data set from AVHRR data Edition 2 (CLARA-A2) during 1979 to 2015 at a spatial
254 resolution of 0.25° was used to compare with the spatiotemporal variability in snow cover
255 calculated from the TPSCE in our study. The CLARA-SAL surface albedo data set is generated
256 based on a homogenized AVHRR radiance time series and is created by using algorithms to
257 derive surface albedo for different land use areas separately, including snow, sea ice, open water,
258 and vegetation. Currently, the CLARA-SAL surface albedo data set is the only available long
259 time-span albedo product derived from AVHRR imagery (Riihelä et al., 2013).

260 **2.1.4. Grid cell definition**

261 A summary of data sets used in this study is listed in Table 4.

262 **Table 4.**

263 Summary of data sets used in this study.

Data purpose	Datasets	Time span	Spatial resolution	Temporal resolution	References
Primary data	AVHRR surface reflectance CDR	1981–present	0.05°	Daily	Vermote et al. (2014)
	MOD10C1	2000–present	0.05°	Daily	Hall et al. (1995)
Ancillary data	MYD10C1	2002–present	0.05°	Daily	Hall et al. (1995)
	IMS	2004–present	4-km	Daily	Helfrich et al. (2007)
	JASMES	1978–2015	5-km	Daily	Hori et al. (2017)
	PSD	1978–2016	25-km	Daily	Che et al. (2008)
	ERA	1972–present	0.125°	Daily	Dee et al. (2011)
	SRTM DEM	–	90-m	–	http://seamless.usgs.gov/
Cross-comparison data	MCD12Q1	2012	0.05°	Yearly	Friedl et al. (2010)
	MCD10A1-TP	2000–2014	500-m	Daily	Huang et al. (2014)
	NHSCE	1966–2015	24-km	Weekly	Robinson et al. (1993)
	CLARA-A2	1979–2015	0.25°	Monthly	Riihelä et al. (2013)
	PERSIANN	1983–2015	0.25°	Daily	Ashouri et al. (2015)

264 To match the spatial resolution of the AVHRR surface reflectance CDR, other data sets were
265 regrided at a spatial resolution of 0.05° and an array resolution of 800×300 pixels with
266 geographic latitude/longitude projection by using the resampling method of "average" or
267 "cubic-spline" with the help of gdalwarp (<http://www.gdal.org/gdalwarp.html>). For data sets with
268 a spatial resolution greater than 0.05°, we used "average" in the resampling process, which
269 computed the average of all non-NODATA contributing pixels in the domain of our study. For
270 data sets with a spatial resolution lower than 0.05°, we used "cubic-spline" in the resampling
271 process. The latitude and longitude of the center of the upper left grid cell were set at 40.0°N and

272 66.0°E according to the location of TP, as shown in Fig. 1. The latitude and longitude data
273 correspond to a center pixel of a 0.05° by 0.05° block of grid cells in the TPSCE.

274 **2.2. Snow discrimination accuracy evaluation**

275 **2.2.1. Evaluation by ground snow-depth observations**

276 Validating moderate-resolution satellite images by field measurements is difficult because a
277 single grid cell from satellite measurements can measure the information from an extremely large
278 area, which may overestimate or underestimate the information from a field measurement.
279 However, the field measurements are still the most convincing records to test the reliability of
280 satellite retrieved products. To estimate the snow discrimination accuracy of the TPSCE, we used
281 snow duration days (D_d) as criteria in comparison with ground snow depth observations (Fig. 2).
282 For a given grid cell, D_d was defined as the number of days in a calendar year with snow cover
283 on the ground.

284 **2.2.2. Evaluation by fine-resolution MCD10A1-TP products**

285 In addition to comparisons with ground snow-depth observations, comparison with higher
286 spatial-resolution images is widely used in the validation of moderate-resolution satellite images,
287 such as by Hall et al. (1995). Compared with the newly developed TPSCE, the MCD10A1-TP
288 represents consistent and objective snow estimates derived from high-resolution optical remote
289 sensing data. Therefore, the MCD10A1-TP was used as the benchmark for the TPSCE. The
290 root-mean-square error (RMSE) and bias were used as criteria to evaluate the relative accuracy
291 of the TPSCE relative to MCD10A1-TP during the period 2001 to 2014. The RMSE and bias of

292 the TPSCE to MCD10A1-TP are expressed as follows:

$$293 \quad RMSE = \sqrt{\frac{1}{n} \sum_{i=1}^n (T_i - M_i)^2} \quad (1)$$

$$294 \quad Bias = \frac{1}{n} \sum_{i=1}^n (T_i - M_i) \quad (2)$$

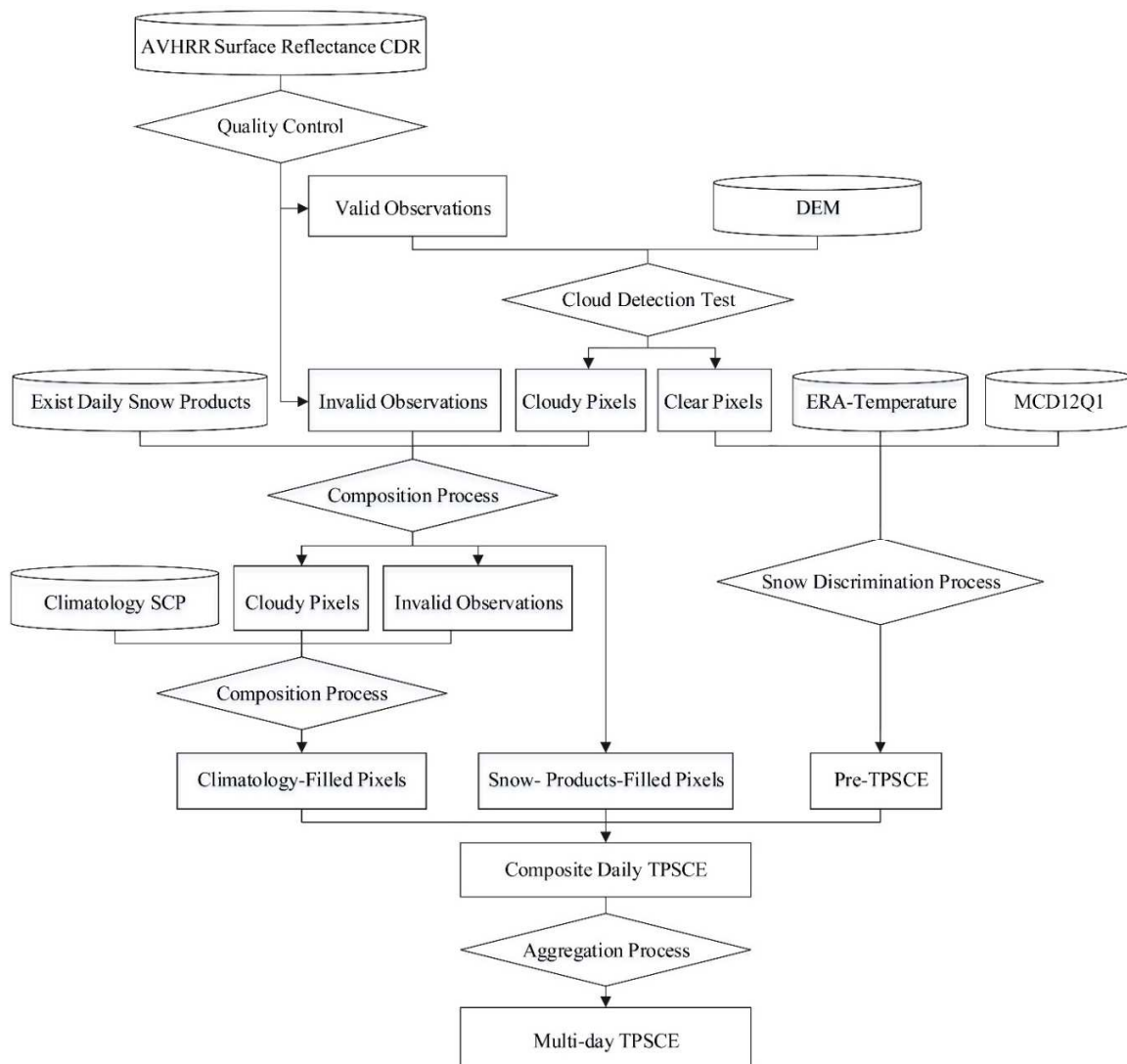
295 where M_i and T_i are the snow cover fraction (SCF) of sample i in the 500-m MCD10A1-TP and
296 5-km TPSCE snow cover products, respectively.

297 **3. Processing Flowchart of TPSCE**

298 **3.1. Flowchart of TPSCE generation**

299 The flowchart of TPSCE generation is presented in Fig. 3. First, by using the quality control flag
300 (Table 2), the grid cells with valid observations in channels 1–5 were employed in the
301 pre-TPSCE generation, in which the quality control flags of "1" in bit 7, indicating channels 1–5
302 that are valid were selected. Second, the cloud detection test was conducted with the help of
303 elevation to reduce the impacts of cloud in the snow discrimination process. The cloud detection
304 test and their threshold values are listed in Table 5. The example of cloud detection test over the
305 study area on December 31, 1981 is presented in Fig. 4. Third, the pre-TPSCE was retrieved
306 from valid AVHRR surface reflectance observations through the snow discrimination process
307 using the decision tree approach. The decision tree and threshold values for snow discrimination
308 are summarized in Fig. 5. The adjustment of NDSI threshold in snow discrimination process is
309 shown in Fig. 6. Fourth, the grid cells with invalid AVHRR surface reflectance observations and
310 cloudy were filled by existing daily snow cover products (including MO/YD10C1, IMS,

311 JASMES, and PSD) through the composition process according to the priority order shown in
 312 Fig. 7. Fifth, the invalid observations and cloudy pixels after the composition process were filled
 313 by the climatology of the snow cover conditions. Examples of pre-TPSCE and TPSCE over the
 314 study area on December 31, 1981 and January 01, 2015 are displayed in Fig. 8. Finally, the
 315 multi-day TPSCE was produced through aggregation of daily TPSCE.



316

317

Fig. 3. Flowchart of TPSCE generation in this study

318 **3.2. Cloud detection test**

319 We did not adopt the cloudy and cloud shadow flag that accompanies the AVHRR surface
 320 reflectance CDR. This is because the cloudy flag appears to overestimate cloudy pixels that exist
 321 in the AVHRR surface reflectance CDR compared with cloudy pixels retrieved from the cloud
 322 detection test used by Hori et al. (2017) and previous studies. To resolve this issue, we employed
 323 the cloud detection test and threshold values according to Hori et al. (2017).

324 **Table 5.**

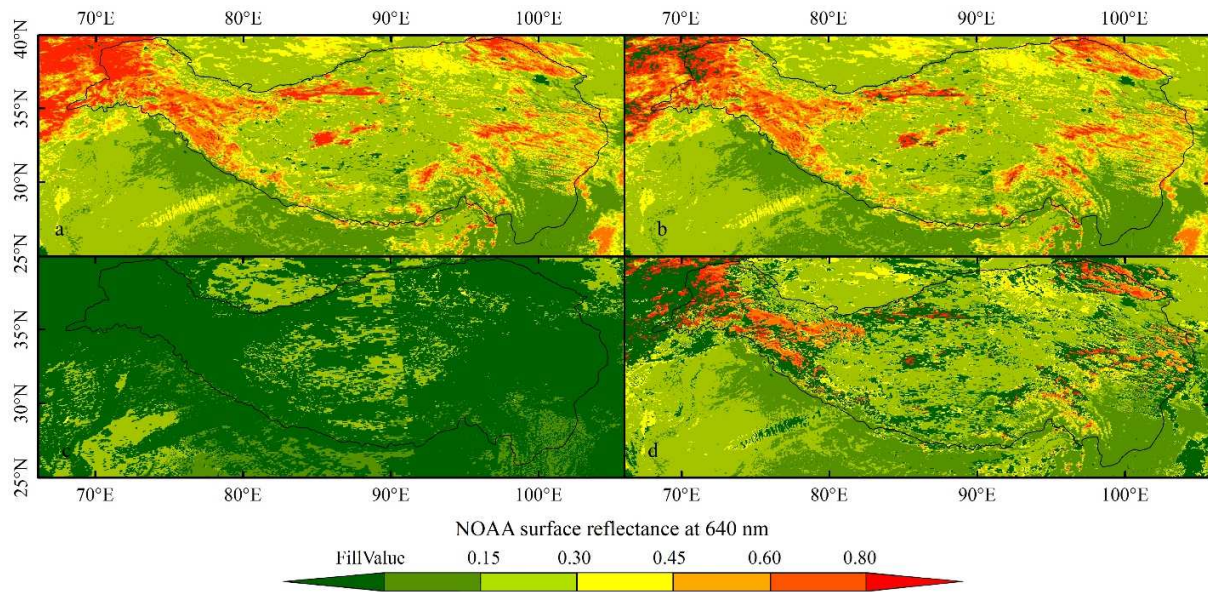
325 Cloud detection tests and their threshold values.

Target	switch	Height (m)	SR1 (-)	SR2 (-)	SR3 (-)	SR1-SR2 (-)	NDVI (-)	NDSI (-)	BT11 (K)	BT37-BT11 (K)	BT11-BT12 (K)
A	on	< 3000							≥ 240	> 8	
	on	≥ 3000							≥ 240	> 15	
B	on								< 240	> 20	
	on				> 0.1	> -0.02		< 0.88			
	off						> 0.5		> 288		
	off								> 310		
	on								< 260	> 8	
	on						> -0.02		< 310	> 10	
B	on		>			> -0.02			< 293	> 9	
			0.3								
	on			> 0.4		> -0.03			< 293	> 8	> -1
	on			> 0.4					< 278	> 20	> -1
on		>			> 0.2			< 263			

		0.3		
off			> 0.5	> 288
off				> 310
off	> 1000	<	< -0.04	> 275
		0.4		
off			< -0.05	> 300

326 This table comes from Hori et al. (2017). Target A indicates high and cold land (elevation > 300 m and BT11 < 260
327 K); Target B indicates other land. The cloud detection test was conducted from the top of the list to the bottom for
328 each target. If the cloudy flag switch was "on", the pixel was set to cloudy when the threshold tests met the
329 conditions listed on the right-hand side. If the switch was "off", the pixel identified as cloudy in the previous tests
330 was reset to clear. $NDVI = (SR2-SR1)/(SR2+SR1)$. $NDSI = (SR1-SR3)/(SR1+SR3)$.

331 Nine variables calculated from the AVHRR surface reflectance CDR (Table 1) were used in the
332 cloud detection test, including SR1, SR2, SR3, BT11, differences between SR1 and SR2
333 (SR1-SR2), differences between BT37 and BT11 (BT37-BT11), differences between BT11 and
334 BT12 (BT11-BT12), the normalized difference vegetation index (NDVI), and NDSI. The cloud
335 detection tests and their threshold values are summarized in Table 5. The differences between the
336 cloudy flag in AVHRR surface reflectance CDR and cloud detection test used by Hori et al.
337 (2017) are shown in Fig. 4. Compared with cloud masked SR1 using cloudy flag (Fig. 4(c)),
338 cloud masked SR1 using the cloud detection algorithm (Fig. 4(d)) provides more reasonable
339 surface reflectance observations.



340

341 **Fig. 4.** (a) Raw AVHRR surface reflectance at 640 nm (SR1), (b) quality controlled SR1 (observations are valid), (c)

342 cloud masked SR1 using cloudy flag, and (d) cloud masked SR1 using the cloud detection algorithm over the study

343 area on December 31, 1981.

344 3.3. Snow discrimination process

345 A snow discrimination process was used to classify the land surface into snow and non-snow.

346 According to the IGBP land cover classification (Fig. 1), grid cells were classified into four types

347 at the start of the snow discrimination flow. The variables and thresholds for snow and non-snow

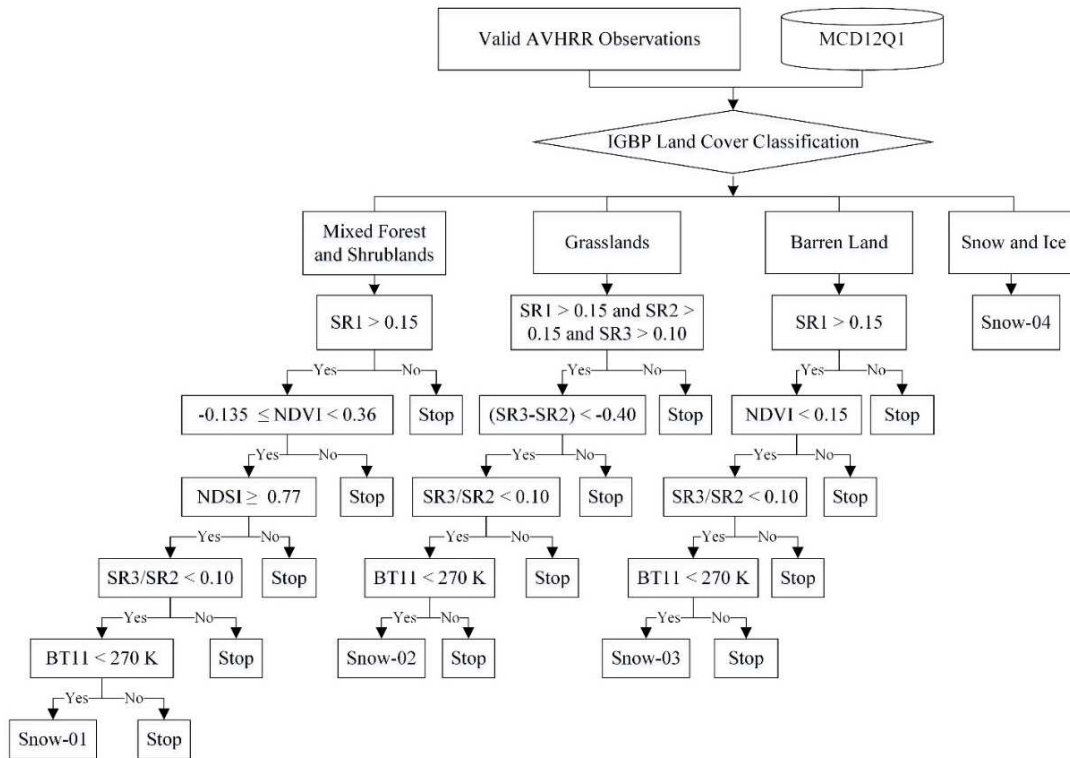
348 discrimination adopted in the decision tree are shown in Fig. 5, in which the pre-TPSCE is

349 defined as the combination of Snow-01 to Snow-04. Most of these threshold values in

350 pre-TPSCE generation were not new but, rather, were combinations of the conventional snow

351 detection tests employed in previous studies (Hori et al., 2017; Khlopenkov and Trishchenko,

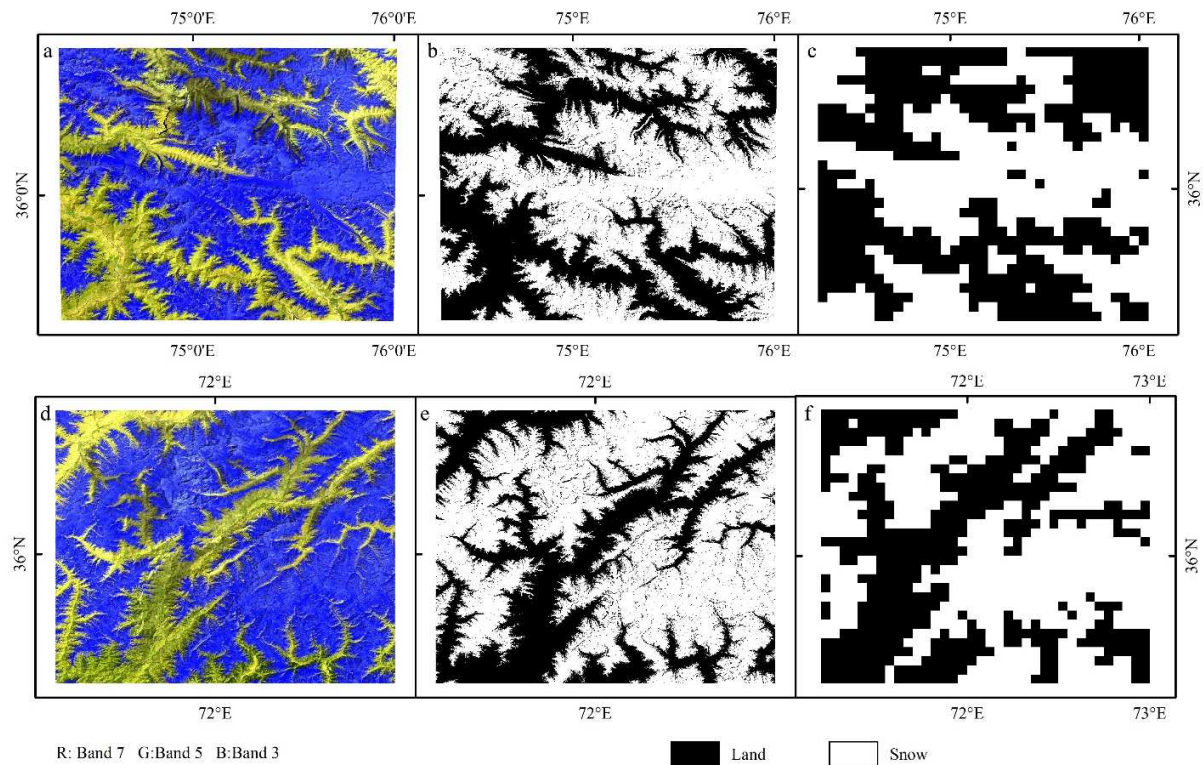
352 2007; Kidder, 1987; Zhou et al., 2013).



353

354 **Fig. 5.** Decision tree and threshold values for snow discrimination using AVHRR surface reflectance CDR

355 As shown by published studies (Hall et al., 1995; Hall et al., 2002), the NDSI could distinguish
 356 effectively between snow and non-snow by referring to the NDVI, particularly in dense
 357 vegetation regions. In Hall et al (1995), the NDSI was calculated by using the red (approximate
 358 wavelength of 630 nm) and shortwave infrared (1.64 μm) bands. As there are no shortwave
 359 infrared observations around the 1.64 μm wavelength in AVHRR surface reflectance CDR, we
 360 used the reflectance at 3.7 μm for an NDSI-like calculation, following Hori et al. (2017).
 361 Moreover, Hori et al. (2017) used 0.80 as the NDSI threshold to develop JASMES using AVHRR
 362 observations over the NH. Given the complex topography and unique snow properties in the TP,
 363 this NDSI threshold needs to be adjusted before used in the pre-TPSCE generation.



364

365 **Fig. 6.** False color images of (a) A and (d) B listed in Table 3. Snow cover extent retrieved by the SNOMAP
 366 algorithm of (b) A and (e) B. Snow cover extent retrieved by AVHRR surface reflectance CDR using an NDSI
 367 threshold of 0.80 of (c) A and (f) B. In the combination of Landsat 5 bands 7, 5, 3 as RGB, snow appears in blue on
 368 the landscape.

369 The comparisons between the SCE retrieved from Landsat 5 TM images and AVHRR surface
 370 reflectance CDR are shown in Fig. 6. The SNOMAP algorithm (Hall et al, 1995) was applied to
 371 retrieve SCE from Landsat 5 TM images. As presented in Fig. 6(b) and (d), SCE was well
 372 mapped by the SNOMAP algorithm compared to the false color images displayed in Figs 6(a)
 373 and 6(c). The snow cover fraction (SCF) of A and B calculated from Landsat 5 TM images are 54%
 374 and 60%, respectively, whereas the SCF of A and B calculated from AVHRR surface reflectance

375 CDR by using 0.80 as the NDSI threshold are 52 % (Fig. 6e) and 56% (Fig. 6f). This means that
 376 using 0.80 as the NDSI threshold may underestimate SCE in the snow discrimination process. To
 377 resolve this issue, we adjusted the NDSI threshold from 0.80 to 0.77 by trial-and-error. In this
 378 case, the SCF of A and B calculated from AVHRR surface reflectance CDR was 55% and 61%,
 379 respectively, which are very similar to those fractions derived from Landsat 5 TM images.

380 3.4. Composition process

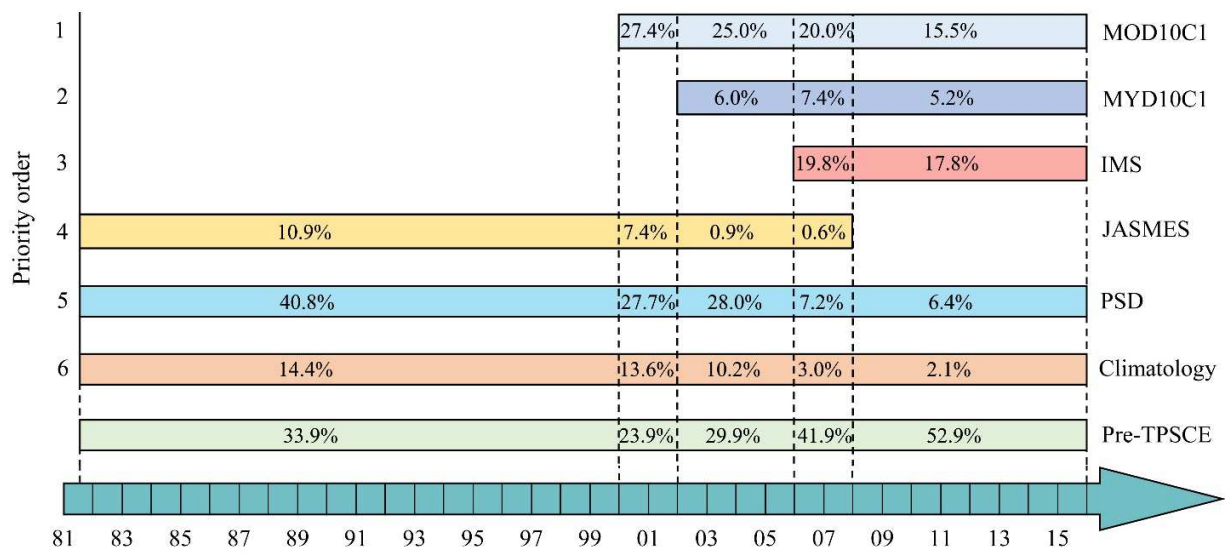
381 To improve the spatial coverage and reduce the omission error of the pre-TPSCE, a composition
 382 process was carried out to fill gaps caused by invalid observations and cloudy pixels. Several
 383 existing daily snow cover products were used in the composite procedure, including
 384 MO/YD10C1, IMS, JASMES, and PSD. The descriptions of the composite TPSCE are
 385 summarized in Table 6.

386 **Table 6.**

387 Descriptions of composite daily TPSCE.

Value	Description	Value	Description
0	Non-snow	5	Pixel is filled by IMS
1	Pre-TPSCE	7	Pixel is filled by JASMES
2	Pixel is filled by MOD10C1	11	Pixel is filled by PSD
3	Pixel is filled by MYD10C1	13	Pixel is filled by Climatology

388 The priority order of integrating these snow cover products with the pre-TPSCE and their
 389 contributions in the daily TPSCE are presented in Fig. 7.

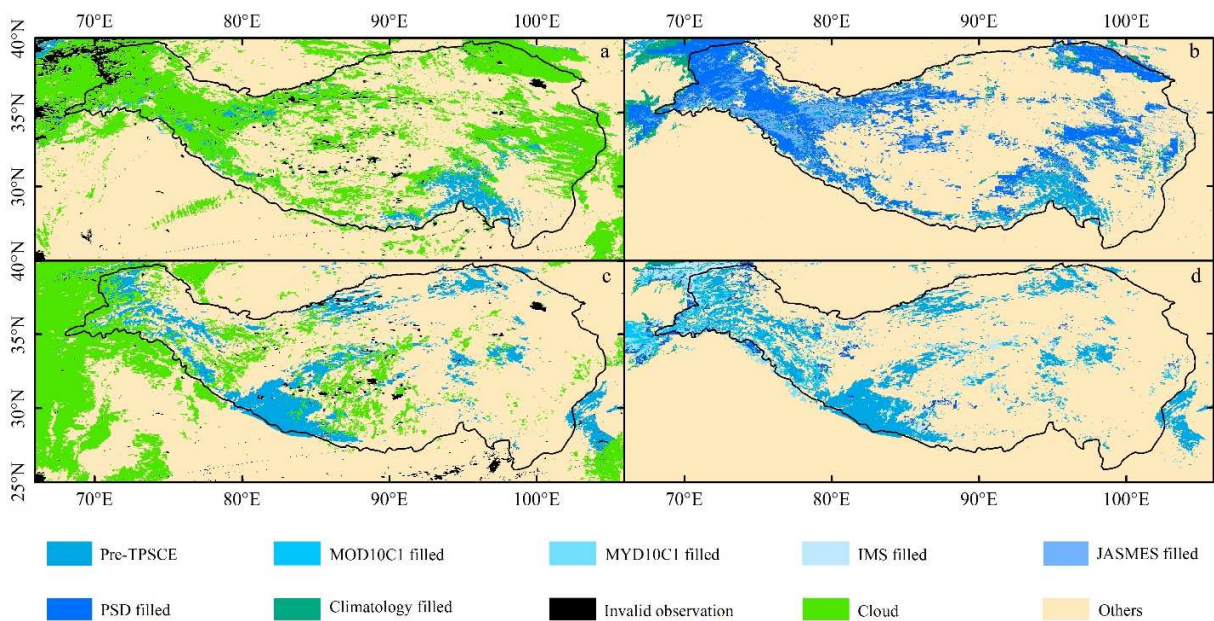


390

391 **Fig. 7.** Priority order of integrating existing snow cover products with the pre-TPSCE and their contributions to the
 392 composite TPSCE.

393 The priority order (Fig. 7) of integrating existing daily snow cover products with the pre-TPSCE
 394 was determined according to their spatial resolution. Compared with other ancillary snow cover
 395 data sets, both MOD10C1 and MYD10C1 represent consistent and objective snow estimates
 396 derived from high-resolution optical remote sensing data. Therefore, the MODIS snow cover
 397 data set was used as the first choice in gap filling for the pre-TPSCE. As the JASMES snow
 398 cover data set used both AVHRR and MODIS radiance data, which is repeated by the existing
 399 MODIS daily snow cover data set, we adopted only the JASMES data derived from AVHRR
 400 GAC radiance data during 1981–2008 in the composition process. In addition, to fill gaps
 401 induced by invalid observations and cloud contamination after the composite process, we
 402 calculated the climatology of daily snow cover probability for each grid cell by using IMS for the
 403 period 2005–2016. For a given grid cell, the snow cover probability in a given period was

404 calculated by the number of years with snow cover divided by the number of years. For gaps that
 405 still exist after the composite process, the climatology of snow cover probability was employed
 406 to discriminate snow from non-snow areas. For grid cells with gaps, the snow cover probability
 407 greater than 50% was masked as snow. Examples of the pre-TPSCE and composite TPSCE on
 408 December 31, 1981 and January 01, 2015 are shown in Fig. 8.



409
 410 **Fig. 8.** Comparisons of (a and c) the pre-TPSCE and (b and d) TPSCE on December 31, 1981 and
 411 January 01, 2015 over the study area.

412 3.5. Aggregation process

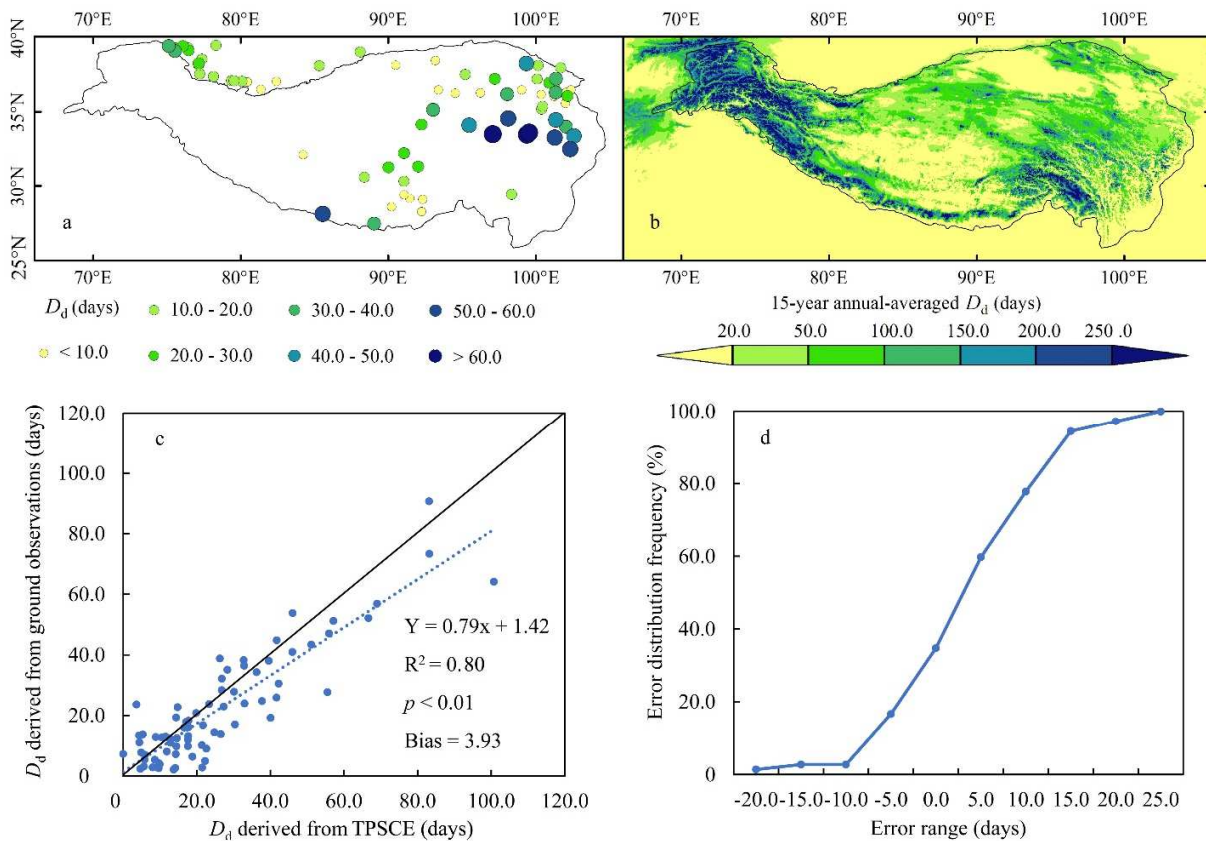
413 In order to compare the TPSCE with the current multi-day snow cover data sets, e.g., the 8-day
 414 MODIS snow cover data set, weekly NHSCE data set, 5-day AMSR-E SWE products, and other
 415 land surface variables, e.g., 5-day CLARA-SAL surface albedo products and 8-day MODIS leaf
 416 area index products, it was necessary to generate composite SCE data sets at varying temporal

417 resolutions. For multi-day TPSCE, only grid cells with snow cover probability greater than or
 418 equal to 50% were defined as snow-covered regions.

419 **4. Snow Discrimination Accuracy of the TPSCE**

420 **4.1. Comparisons with ground snow-depth observations**

421 Subject to the data availability of CMA snow-depth observations, the comparison between the
 422 TPSCE and snow-depth observations was carried out during 2000–2014. The climatology of D_d ,
 423 calculated from the TPSCE and 72 ground snow-depth observations across the TP for the period
 424 2000–2014 is shown in Fig. 9.



425
 426 **Fig. 9.** Climatology of snow duration days D_d calculated from (a) 72 in situ snow-depth observations, and (b) the
 28

427 TPSCE across the TP for the period 2000–2014. (c) Comparisons between the climatology of D_d calculated from the
428 TPSCE and in situ observations. (d) Error distribution frequency of D_d calculated from the TPSCE across the TP for
429 the period 2000–2014.

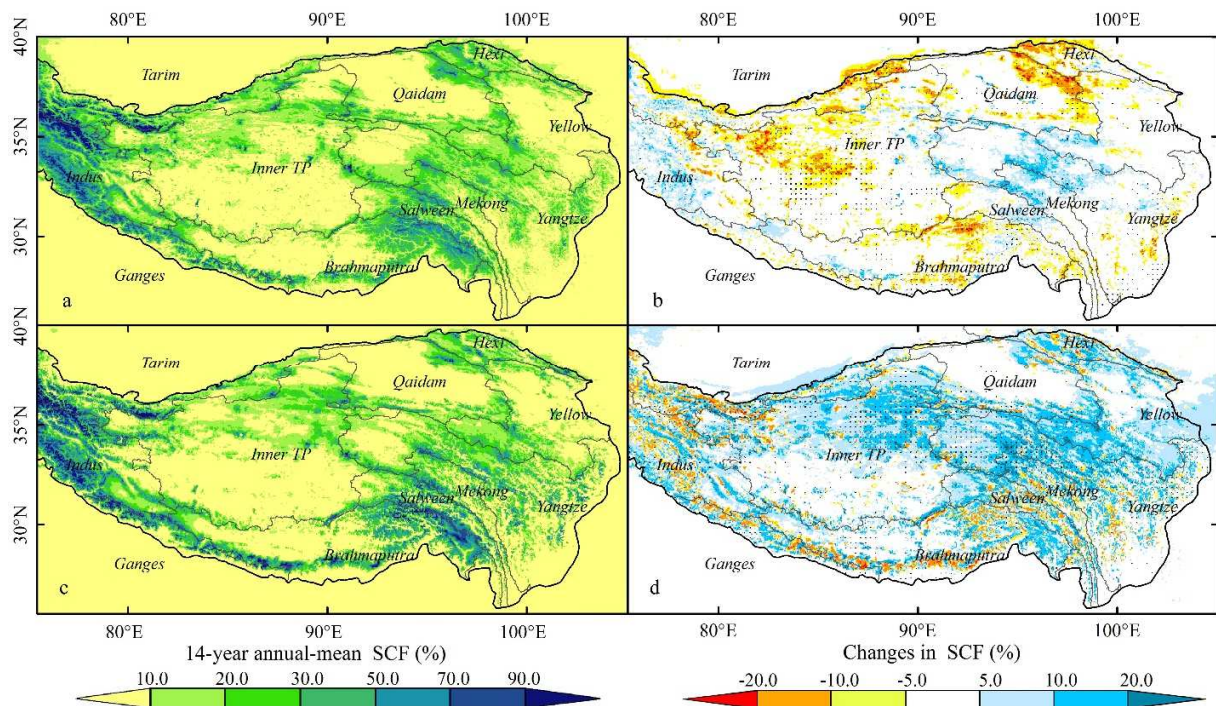
430 Fig. 9(a) shows the spatial patterns of the 15-year climatology of D_d over the CMA-covered
431 stations during 2000–2014. There are clear altitudinal gradient patterns for D_d from low to high
432 altitudes. At most sites, the observed D_d is consistent with the TPSCE-retrieved D_d results
433 (Fig. 9(b)), with an R^2 value of 0.80 at the 99% significant level. However, the bias in the
434 TPSCE-retrieved D_d and the observed D_d is positive, with a value of 3.93 days (Fig. 9(c)), which
435 means that the TPSCE tends to overestimate actual D_d across the TP during 2000–2014.
436 Moreover, as shown in Fig. 9(c), TPSCE-retrieved D_d is higher than the ground observed D_d ,
437 particularly in the lower end of the D_d scale. These phenomena were caused mainly by the low
438 spatial resolution of the TPSCE, which provide the averaged D_d value at the pixel scale. As the
439 spatial resolution of the TPSCE is limited, the minima units in the TPSCE-retrieved D_d are pixels
440 at 0.05° , which cannot catch and reflect entirely the actual (real) D_d at a specific spot location.

441 The error distribution frequency of the differences between the TPSCE-retrieved D_d and the in
442 situ observed D_d (TPSCE-retrieved D_d minus in situ observed D_d) is shown in Fig. 9(d). The
443 overestimated D_d accounts for 65.2% of the total 72 stations used in this study, in which 25% and
444 18% of the stations distributed an error range between 0–5 days and 5–10 days, respectively.
445 Previous research has shown that the raw in situ observations would give results that depend
446 highly on a particular location (latitude and elevation) (Hansen et al., 2010). Such results would

447 reflect mostly those accidental snow circumstances, rather than yield meaningful climatology
448 value of D_d . However, as shown in Fig. 9, D_d retrieved by the TPSCE still skillfully captures the
449 D_d distributions over the TP. Although the TPSCE generally overestimates D_d across the TP, the
450 bias (3.93 days) is still acceptable in snow phenology studies compared with other long-term
451 multi-day snow cover products, such as weekly NHSCE.

452 **4.2. Comparisons with fine-resolution MCD10A1-TP**

453 Subject to the spatial coverage and time span of MCD10A1-TP, the comparison between TPSCE
454 and fine-resolution MCD10A1-TP was confined to the overlap regions. The climatology of and
455 changes in SCF calculated from the TPSCE and MCD10A1-TP for the period 2001–2014 across
456 the TP are shown in Fig. 10. In this study, the changes are expressed as linear trends multiplied
457 by the time interval.



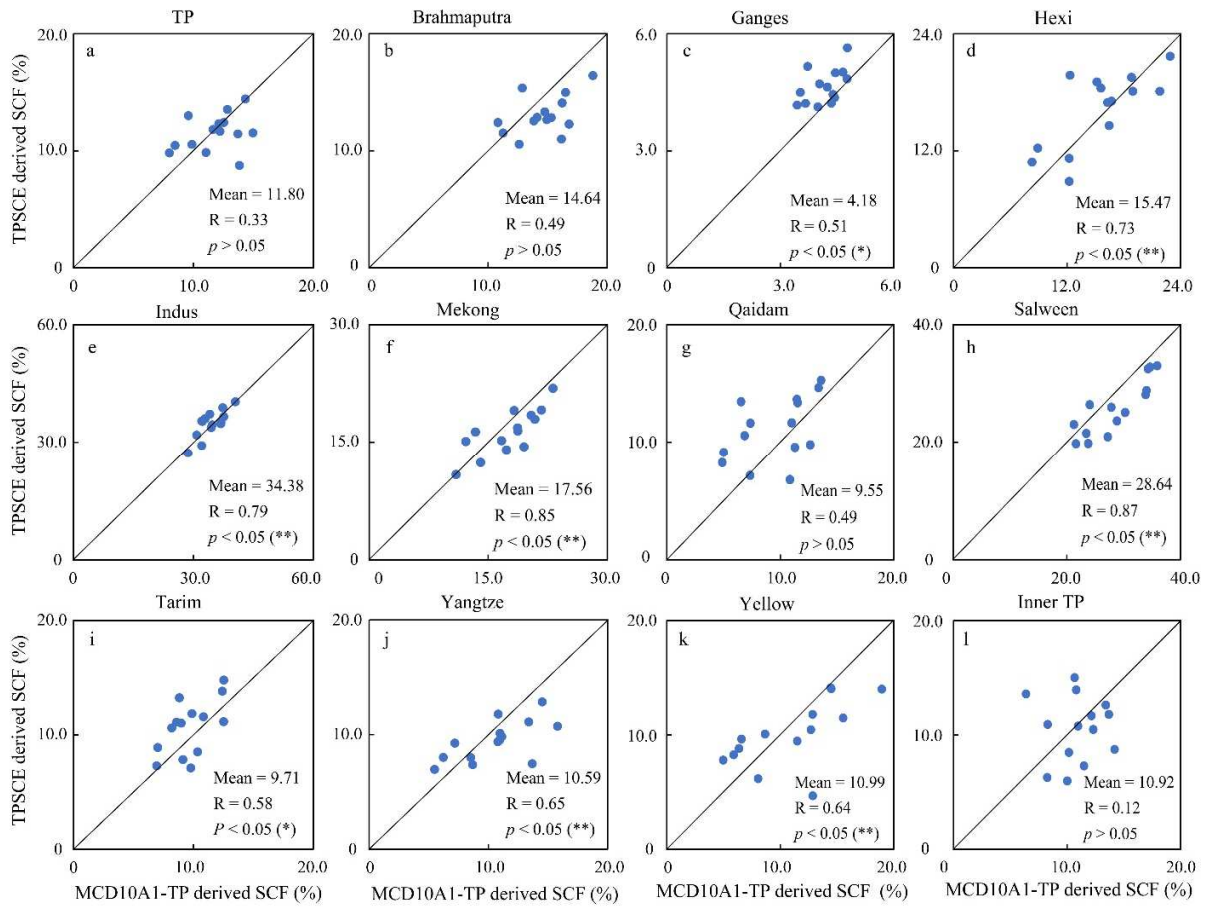
458

459 **Fig. 10.** Climatology of SCF (%) calculated from (a) MCD10A1-TP and (c) TPSCE for the period 2001–2014 across
 460 the TP and each basin for the period 2001–2014. Changes in SCF (%) were calculated from (b) MCD10A1-TP and
 461 (d) TPSCE across the TP and each basin for the period 2001–2014. Black spots in (b) and (d) indicate that the
 462 changes are statistically significant at the 95% level.

463 The spatial distributions of the SCF climatology derived from MCD10A1-TP (Fig. 10(a)) and the
 464 TPSCE (Fig. 10(c)) are similar during 2001–2014, with high SCF values distributed mainly in
 465 the upper reaches of the Tarim, Indus, Brahmaputra, Salween, and Mekong River basins, and the
 466 low SCF values distributed in the Inner TP and Qaidam River basins. However, compared with
 467 the MCD10A1-TP-derived SCF maps, the SCF values in the high-altitude southern margin of the
 468 Brahmaputra River basin and the western Pamir regions were overestimated in the TPSCE SCF
 469 maps. This overestimation was caused mainly by a relatively low spatial resolution in the newly

470 developed TPSCE data set, resulting in overestimated (underestimated) SCF values in regions
471 with heavy (low) snow distribution. In addition, both MCD10A1-TP and TPSCE are generated
472 by integrating optical and passive microwave snow data. Thus, uncertainties in the
473 MCD10A1-TP and TPSCE caused by coarse spatial resolution of passive microwave remote
474 sensing, ground temperature, snow characteristics and topography (Dai et al., 2017; Tsutsui and
475 Koike 2012) may also result in the discrepancies between MCD10A1-TP and TPSCE.

476 Variations in SCF derived from MCD10A1-TP (Fig. 10(b)) and TPSCE (Fig. 10(d)) show
477 marked spatial differences from 2001 through 2014. Compared with the changes calculated from
478 MCD10A1-TP, SCF increased not only in the upper reaches of the Yangtze, Mekong, and
479 Brahmaputra River basins, but also in the northern Inner TP river basins, as shown in the change
480 maps calculated from the TPSCE. Since the changes calculated from MCD10A1-TP and TPSCE
481 for the period 2001–2014 are not statistically significant, as indicated in Figs 10(b) and 10(d),
482 owing to the short time interval, we do not present a detailed analysis of the spatial differences in
483 this study. However, to explore the detail of the similarities and differences between
484 MCD10A1-TP and TPSCE, we summarize the comparisons between the annual-mean SCF
485 calculated from MCD10A1-TP and TPSCE for each basin (Fig. 11), with the RMSE and bias
486 listed in Table 7.



487
 488 **Fig. 11.** Linear correlations between annual-mean SCF (%) calculated from MCD10A1-TP and TPSCE for the
 489 period 2001–2014 in (a) entire TP, (b) Brahmaputra, (c) Ganges, (d) Hexi, (e) Indus, (f) Mekong, (g) Qaidam, (h)
 490 Salween, (i) Tarim, (g) Yangtze, (k) Yellow, and (l) Inner TP. * indicates the linear correlation is significant at the 95%
 491 level, ** indicates the linear correlation is significant at the 99% level, whereas the others are not significant at the
 492 95% level.

493 The annual-mean SCF calculated from MCD10A1-TP and TPSCE generally shows positive
 494 linear correlations across the entire region and each basin for the period 2001–2014 (Fig. 11),
 495 with a maximum correlation coefficient ($r = 0.85$, $p < 0.05$) in the Mekong River basin and a
 496 minimum correlation coefficient ($r = 0.12$, $p > 0.05$) in the Inner TP river basins. For basins with

497 snow distribution (e.g., Indus, Mekong, and Salween), the TPSCE could capture the snow
 498 information adequately. However, subject to a 5-km spatial resolution, the TPSCE could not
 499 identify snow cover grid cells accurately in sparse snow cover regions (e.g., Inner TP and
 500 Qaidam).

501 **Table 7.**

502 RMSE and bias for SCF (%) calculated from the TPSCE and MCD10A1-TP across the TP and each basin for the
 503 period 2001–2014.

Basin	RMSE (%)	Bias (%)	Basin	RMSE (%)	Bias (%)
TP	2.15	-0.25	Mekong	2.51	-1.26
Brahmaputra	2.53	-1.58	Qaidam	3.27	1.52
Ganges	0.64	0.47	Salween	3.79	-2.80
Hexi	3.04	0.71	Tarim	2.16	0.92
Yellow	3.31	-0.93	Inner TP	3.44	-0.37
Indus	2.14	0.40	Yangtze	2.56	-1.13

504 As shown in Table 7, we found large differences in RMSE and bias among the basins across the
 505 TP for the period 2001–2014. The RMSE between the TPSCE SCF series and the MCD10A1-TP
 506 SCF series was 2.15% over the entire TP during the period, ranging from 0.64% in the Ganges
 507 River basin to 3.79% in the Salween River basin. In addition, the bias between the TPSCE SCF
 508 series and the MCD10A1-TP SCF series over the entire TP for the period was -0.25%, with a
 509 maximum underestimated SCF (-2.80%) in the Salween River basin and a maximum
 510 overestimated SCF (1.52%) in the Qaidam River basin.

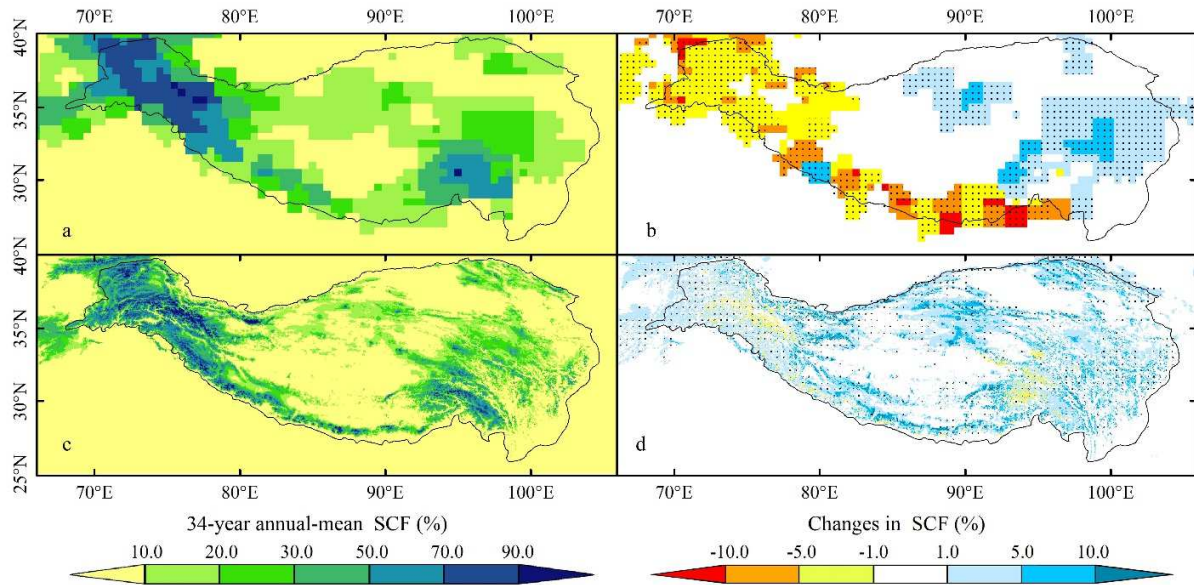
511 **5. Cross-comparison between snow cover from TPSCE and other climate variables**

512 **5.1. Long-term snow cover changes derived from TPSCE**

513 The long-term snow cover changes derived from the TPSCE and NHSCE from 1982 to 2015
514 were compared. To match the temporal resolution of the weekly NHSCE data set, the aggregated
515 weekly TPSCE were used. The climatology and changes in SCF derived from the NHSCE and
516 TPSCE data sets across the TP for the period 1982–2015 are presented in Fig. 12. Because the
517 time series of the TPSCE is incomplete due to data missing of AVHRR surface reflectance in
518 1994, we excluded this year in detection of long-term changes in snow cover and
519 cross-comparisons with other climate variables in this study.

520 The 34-year climatology of the annual-mean SCF calculated from NHSCE (Fig. 12(a)) and
521 TPSCE (Fig. 12(c)) is similar in spatial distribution during 1982–2015. However, the
522 climatology of the annual-mean SCF calculated from the TPSCE demonstrates more detailed
523 information on long-term SCF conditions across the TP. Compared with the SCF maps calculated
524 from TPSCE, the SCF values in the southeast Brahmaputra River basins and northwest Pamirs
525 were overestimated in the NHSCE SCF maps. In addition to the low spatial resolution of the
526 NHSCE snow cover products, the definition of snow cover in the NHSCE snow cover products
527 also contributes to this deviation. According to Helfrich et al. (2007) and Brown and Robinson
528 (2011), the grid cell was marked as 0 or 1 in the NHSCE snow cover products, with $<50\%$ or \geq
529 50% snow occurrence probability, respectively. This definition of snow cover in the NHSCE data
530 set could result in overestimated SCF values in regions with heavy snow but underestimated SCF

531 values in regions with patchy snow. This is because NHSCE could only detect grid cells with \geq
 532 50% snow occurrence probability effectively, whereas the patchy snow could not be identified
 533 well.



534
 535 **Fig. 12.** 34-year climatology of annual-mean SCF (%) across the TP for the period 1982–2015 (excluding 1994),
 536 calculated from (a) NHSCE and (c) TPSCE. The 34-year changes in SCF (%) were calculated from (b) NHSCE and
 537 (d) TPSCE. Black dots in (b) and (d) indicate changes that are significant at the 95% level.

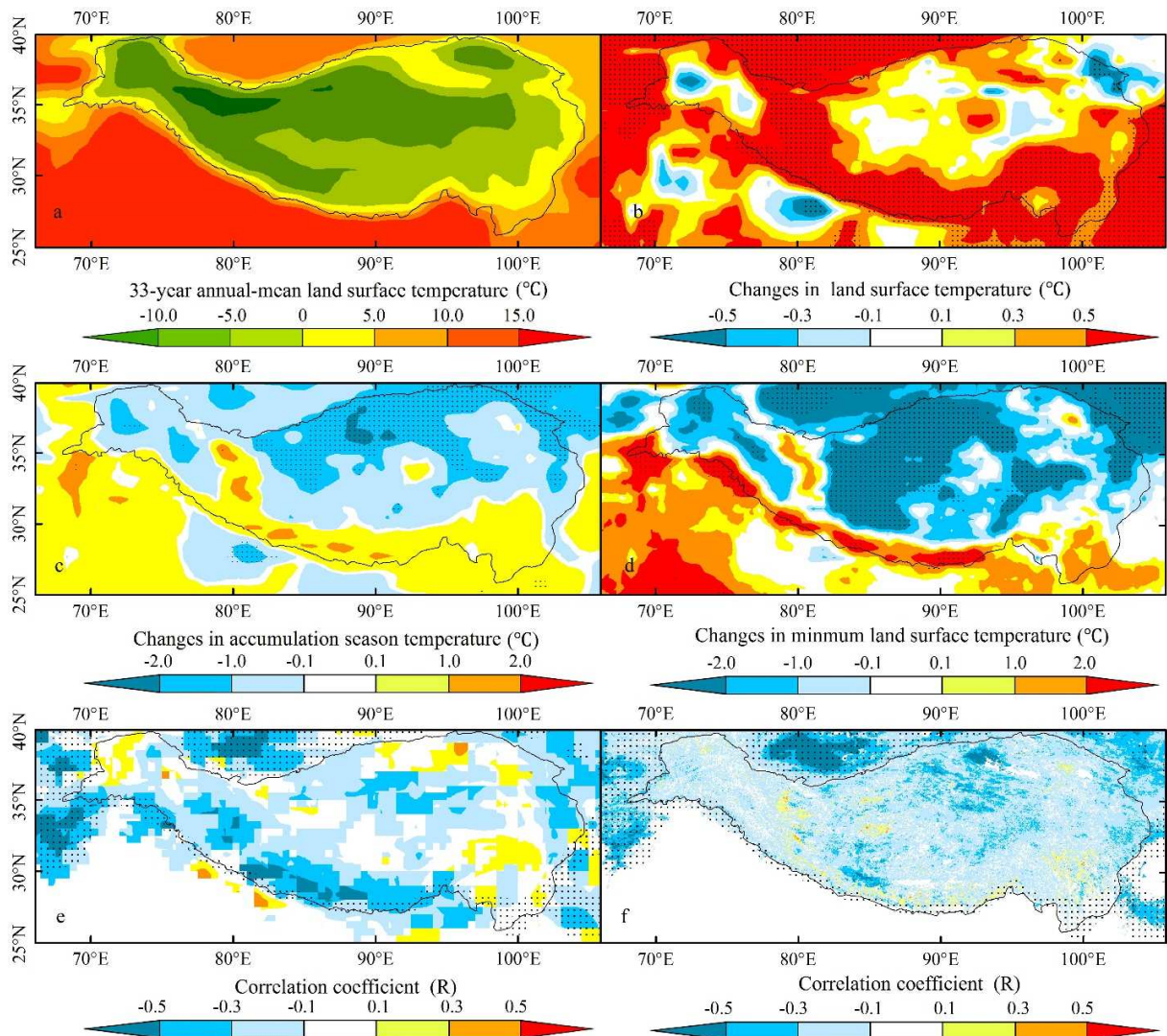
538 The response of SCF to climate change can be demonstrated well by long-term SCF changes.
 539 Variations in SCF calculated from NHSCE (Fig. 12(b)) and TPSCE (Fig. 12(d)) show large
 540 spatial differences across the TP during 1982–2015, especially in the Pamirs and the southern
 541 margin of the TP. In contrast with a significant SCF decrease in the Brahmaputra River basin, as
 542 shown in Fig. 12(b), the SCF increases in most areas of the Brahmaputra River basin, as shown
 543 in Fig. 12(d). Climatic variables, including temperature and precipitation, were considered the

544 contributing factors to these SCF changes. However, previous studies focused mainly on snow
545 cover changes in northern high latitudes, with the actual conditions of snow cover and the
546 driving forces in mid-latitudes over a long time span discussed only rarely. To solve the lack of
547 references in evaluating the reliability of long-term NHSCE and TPSCE, we conducted
548 cross-comparison as discussed in the following sections.

549 **5.2. Cross-comparison between snow cover and land surface temperature**

550 The cross-comparison between SCF and land surface temperature during 1982–2016 was
551 conducted (Fig. 13). Based on the annual cycle of SCF over the TP from 2001 to 2014 ([Chen et](#)
552 [al., 2017](#)), snow cover increased from September to February, with SCF increasing significantly
553 in December and January. To compare the changes in temperature and SCF, this study used the
554 December–January average accumulation season temperature and the minimum temperature.

555 As shown in Fig. 13(b), the 33-year annual-mean land surface temperature shows a warmer trend
556 in most of the regions across the TP for the period 1982–2016 (excluding 1994). However, in
557 contrast with the changes in the annual-mean temperature, both accumulation season temperature
558 (Fig. 13(c)) and minimum temperature (Fig. 13(d)) show a generally cooler trend across the TP
559 during 1982–2016 (excluding 1994). This is beneficial to snow accumulation on the ground and
560 could have resulted in longer-duration snow cover and increased SCF. The cooler accumulation
561 season temperature and the lower minimum temperature across the TP are consistent partly with
562 the long-term tendency of large-scale cooling trends in land surface temperature during winter
563 over mid-latitudes that have been observed since approximately the 1990s ([Cohen et al., 2014](#);



565

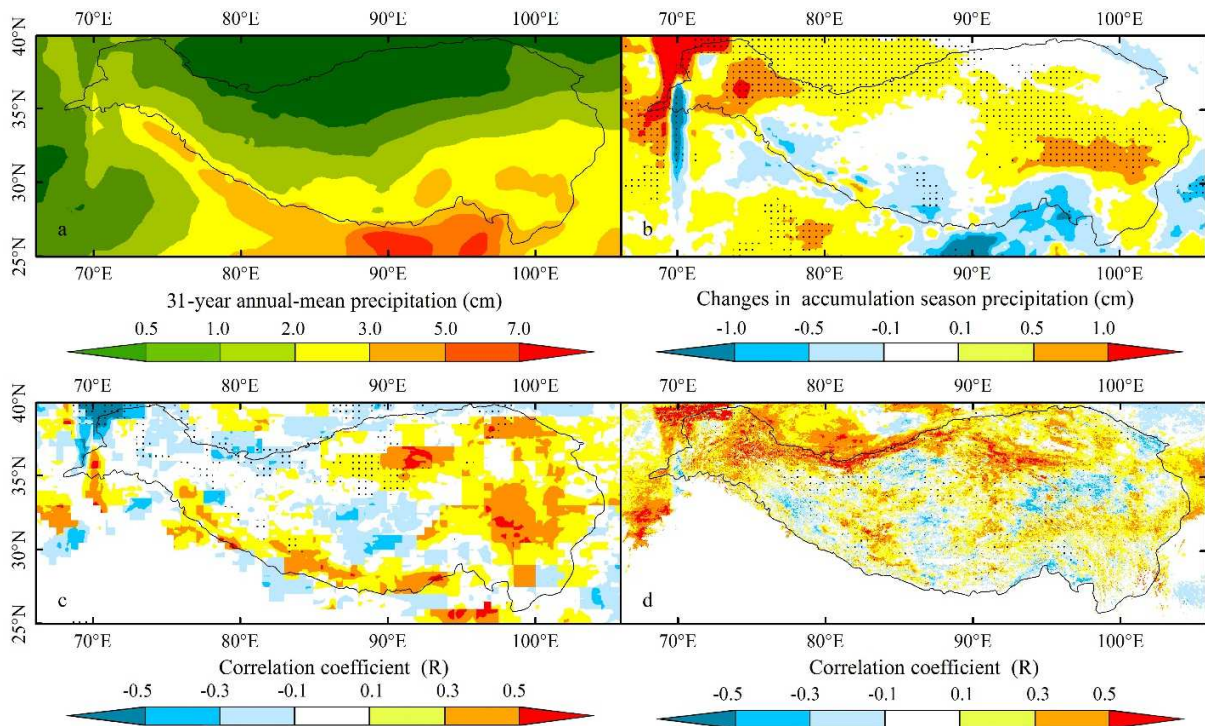
566 **Fig. 13.** 33-year (a) climatology of annual-mean land surface temperature (°C) and changes in (b) annual-mean land
 567 surface temperature (°C), (c) accumulation season temperature, and (d) minimum land surface temperature across
 568 the TP for the period 1982–2016 (excluding 1994). The correlation coefficient (R) between land surface temperature
 569 and SCF calculated from (e) NHSCE and (f) TPSCE snow cover products. Black dots in (b), (c), and (d) indicate
 570 that changes are significant at the 95% level. Black dots in (e) and (f) indicate that the correlation coefficients are
 571 statistically significant at the 95% level.

572 Maps of the correlation between the accumulation season temperature and NHSCE and the
573 TPSCE are shown in Figs 13(e) and 13(f), respectively. A generally negative correlation between
574 the accumulation season temperature and SCF is indicated for most regions of the study area, as
575 shown in Figs 13(e) and 13(f). However, the TPSCE provides superior results in the Pamirs
576 because of the erroneous positive correlation between the accumulation season temperature and
577 SCF calculated from the NHSCE. Meanwhile, in the south margin of the TP with high
578 annual-mean SCF, the NHSCE provides better correlation with accumulation season temperature
579 compared with the TPSCE.

580 **5.3. Cross-comparison between snow cover and accumulation season precipitation**

581 In addition to the accumulation season temperature, precipitation plays a critical role in snow
582 accumulation on the ground. The cross-comparison between snow cover and accumulation
583 season precipitation during 1983–2015 was conducted (Fig. 14). As shown in Fig. 14(b),
584 accumulation season precipitation increases in most of the central and eastern TP during 1983–
585 2015 (excluding 1994), which is beneficial to snow accumulation on the ground and could have
586 resulted in deeper snow cover and a longer snow season. This pattern coincides with the previous
587 findings on large-scale cold snaps, heavy snowfall, and glacier events at middle latitudes since
588 the 1990s (Cohen et al., 2010; Cohen et al., 2012; Yao et al., 2012). Furthermore, the SCF was
589 shown to be correlated positively with the accumulation season precipitation, as demonstrated in
590 Figs 14(c) and 14(d). Compared with Fig. 14(d), the correlation between the accumulation
591 season precipitation and SCF derived from the NHSCE (Fig. 14(c)) shows poor results in the

592 western TP and, particularly, the Pamirs. However, in the eastern and southern margins of the TP,
 593 the performance of the NHSCE is better than the TPSCE.

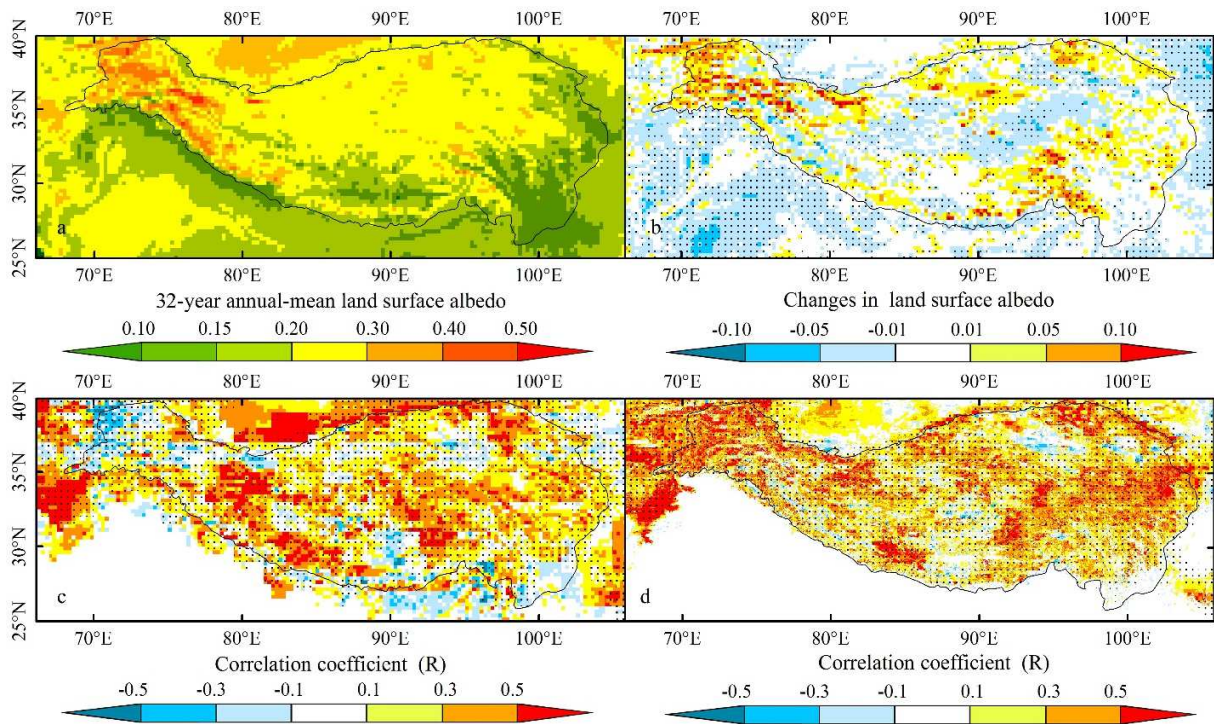


594
 595 **Fig. 14.** 31-year (a) climatology of annual-mean precipitation (cm) and (b) changes in accumulation season
 596 precipitation across the TP for the period 1983–2015 (excluding 1994). The correlation coefficient (R) between
 597 accumulation season precipitation and SCF is calculated from (c) NHSCE and (d) TPSCE snow cover products.
 598 Black dots in (b) indicate that changes are significant at the 95% level. Black dots in (c) and (d) indicate that the
 599 correlation coefficient is statistically significant at the 95% level.

600 **5.4. Cross-comparison between snow cover and land surface albedo**

601 Land surface albedo has been shown to be related closely with snow cover changes because of
 602 the highly reflective surface of snow cover. The cross-comparison between snow cover and land

603 surface albedo during 1982–2015 was conducted. The 32-year climatology of the annual-mean
 604 land surface albedo and changes across the TP for the period 1982–2015 (excluding 1994)
 605 calculated from the CLARA-SAL are shown in Fig. 15.



606
 607 **Fig. 15.** 32-year (a) climatology of annual-mean land surface albedo and (b) changes across the TP for the period
 608 1982–2015 (excluding 1994). The correlation coefficient (R) between land surface albedo and SCF was calculated
 609 from (c) NHSCE and (d) TPSCE snow cover products. Black dots in (b) indicate that changes are significant at the
 610 95% level. Black dots in (c) and (d) indicate that the correlation coefficient is statistically significant at the 95%
 611 level.

612 The distribution of 32-year annual-mean land surface albedo across the TP from 1982 to 2015
 613 (excluding 1994) (Fig. 15(a)) is similar to the climatology of the annual-mean SCF distribution
 614 shown in Fig. 12. Moreover, changes in land surface albedo partly represent snow cover changes

615 according to Chen et al. (2017). As shown in Fig. 15(b), the land surface albedo shows an
616 increasing trend in the Pamirs and Brahmaputra River basin, which is the opposite of the
617 decreasing SCF calculated from the NHSCE snow cover maps (Fig. 12(b)). Moreover, compared
618 with Fig. 15(c), the correlation coefficients between the land surface albedo and SCF calculated
619 from the TPSCF were more reasonable, especially in the Pamirs. By comparison with long-term
620 changes in temperature, precipitation, and land surface albedo, we found that the performance of
621 the newly developed TPSCE is superior compared with that of the widely used NHSCE snow
622 cover products in capturing long-term snow cover anomalies across the TP.

623 **6. Summary and Conclusion**

624 The long-term snow cover condition across the TP has not been well documented owing to
625 limited data availability. Using AVHRR surface reflectance CDR and several existing snow cover
626 products, we generate a composite daily SCE record of the TP from 1981 to 2016. The newly
627 developed TPSCE has several advantages in TP snow cover studies, including long time series,
628 high and temporal spatial resolution, and complete spatial coverage, compared with NHSCE and
629 GlobSnow with low spatial resolution, Suomi-NPP and MODIS with short time span, and
630 JASMES with incomplete coverage. This data set facilitates a novel report on the evolution of
631 snow cover across the TP during three decades (1981 to 2016) as a peculiar mid-latitude
632 cryosphere.

633 Validation results of the daily TPSCE against ground snow-depth observations and the
634 fine-resolution MCD10A1-TP snow cover show high snow discrimination accuracy of the

635 TPSCE. Comparisons of SCF distribution and historical change analysis across the entire TP and
636 nine river basins (e.g. Brahmaputra, Ganges, Hexi, Indus, Mekong, Qaidam, Salween, Tarim,
637 Yangtze, Yellow, and Inner TP) from 2001 to 2014 provide the RMSE and bias between the
638 newly developed TPSCE and the fine-resolution MCD10A1-TP in SCF quantification over the
639 TP, and show that the TPSCE could capture snow distribution skillfully. The cross-comparisons
640 between the SCF anomaly derived from the TPSCE and changes in land surface temperature,
641 precipitation, and albedo further show the reliability of the newly developed TPSCE data set.
642 Compared with the correlation between the SCF calculated from the NHSCE data set and the
643 land surface temperature, precipitation, and albedo, the SCF calculated from the TPSCE presents
644 a superior performance.

645 This long-term composite snow cover data set is suited for studying seasonal snow cover across
646 the TP and could present a unique opportunity for climatological and hydrological studies on
647 seasonal snow cover and surface water resource changes in the TP over the past three decades.
648 However, some issues remain in the newly developed TPSCE data set, such as lower confidence
649 of snow cover before 2000 compared with that after 2000, few ground snow-depth observations
650 in regions with heavy snow distribution, and a confined study area limited by the availability of
651 ancillary data. Cloud contamination is one of the most difficult aspects in snow cover
652 discrimination when using optical remote sensing images. However, with the utility of historical
653 passive microwave images and the development of the cloud detection approach, long-term,
654 high-quality, and fine-resolution snow cover products are expected in the future.

655 **Acknowledgements**

656 This study was funded by the National Natural Science Foundation of China (under grant No.
657 91547210, No. 51722903, and No. 91437214), the National Key Research and Development
658 Program of China (under grant No. 2016YFE0102400 and 2016YFA0600103), and China's
659 Postdoctoral Science Foundation (under grant No. 2016M600080). All colleagues involved in
660 producing this data set are highly appreciated. The AVHRR surface reflectance CDR and the
661 PERSIANN precipitation CDR are available at the National Climatic Data Center
662 (<https://www.ncdc.noaa.gov/>). The MCD10A1-TP snow cover products are provided by the
663 Northwest Institute of Eco-Environment and Resources, Chinese Academy of Sciences
664 (<http://westdc.westgis.ac.cn/data>). The MODIS, NHSCE, and IMS snow cover products are
665 obtained from the National Snow and Ice Data Centre (<http://nsidc.org/data/G02156>). The
666 JASMES snow cover products are obtained from the Japan Aerospace Exploration Agency
667 (<http://kuroshio.eorc.jaxa.jp/JASMES/datalist.html>). The ERA-Interim temperature data sets are
668 available at the European Centre for Medium-Range Weather Forecasts
669 (<https://www.ecmwf.int/>). The MCD12Q1 land cover products are available at the LAND
670 Processes Distributed Active Archive Centre (<https://lpdaac.usgs.gov/>). The SRTM DEM is
671 available at <http://seamless.usgs.gov/>. The ground observations are available at the
672 Meteorological Data Centre of the China Meteorological Administration (<http://data.cma.cn/>).
673 Reviewers and editors' comments that are valuable for improving this study and manuscript are
674 acknowledged. The TPSCE data set generated from this study is available upon reasonable

675 request (dlong@tsinghua.edu.cn).

676 **References**

- 677 Ashouri, H., Hsu, K.-L., Sorooshian, S., Braithwaite, D.K., Knapp, K.R., Cecil, L.D., Nelson, B.R., & Prat, O.P.
678 (2015). PERSIANN-CDR: Daily precipitation climate data record from multisatellite observations for
679 hydrological and climate studies. *Bull. Amer. Meteor. Soc.*, 96, 69-83.
680 <https://doi.org/10.1175/BAMS-D-13-00068.1>
- 681 Brown, R., Derksen, C., & Wang, L. (2010). A multi-data set analysis of variability and change in Arctic spring
682 snow cover extent, 1967–2008. *J. Geophys. Res. Atmos.*, 115, D16111
- 683 Brown, R.D., & Robinson, D.A. (2011). Northern Hemisphere spring snow cover variability and change over 1922–
684 2010 including an assessment of uncertainty. *Cryosphere*, 5, 219-229. <https://doi.org/10.5194/tc-5-219-2011>.
- 685 Che, T., Li, X., Jin, R., Armstrong, R., & Zhang, T. (2008). Snow depth derived from passive microwave
686 remote-sensing data in China. *Ann. Glaciol.*, 145-154.
- 687 Chen, C., Lakhankar, T., Romanov, P., Helfrich, S., Powell, A., & Khanbilvardi, R. (2012). Validation of
688 NOAA-Interactive Multisensor Snow and Ice Mapping System (IMS) by comparison with ground-based
689 measurements over continental United States. *Remote Sens.*, 4, 1134-1145.
- 690 Chen, X., Liang, S., Cao, Y., He, T., & Wang, D. (2015). Observed contrast changes in snow cover phenology in
691 northern middle and high latitudes from 2001-2014. *Sci Rep*, 5, 16820.
- 692 Chen, X., Long, D., Hong, Y., Liang, S., & Hou, A. (2017). Observed radiative cooling over the Tibetan Plateau for
693 the past three decades driven by snow-cover-induced surface albedo anomaly. *J. Geophys. Res. Atmos.*, 122,

694 6170–6185.

695 Cohen, J., Foster, J., Barlow, M., Saito, K., & Jones, J. (2010). Winter 2009-2010: A case study of an extreme Arctic
696 Oscillation event. *Geophys. Res. Lett.*, 37, 2010GL044256.

697 Cohen, J., Screen, J.A., Furtado, J.C., Barlow, M., Whittleston, D., Coumou, D., Francis, J., Dethloff, K., Entekhabi,
698 D., Overland, J., & Jones, J. (2014). Recent Arctic amplification and extreme mid-latitude weather. *Nat.*
699 *Geosci.*, 7, 627-637.

700 Cohen, J.L., Furtado, J.C., Barlow, M.A., Alexeev, V.A., & Cherry, J.E. (2012). Arctic warming, increasing snow
701 cover and widespread boreal winter cooling. *Environ. Res. Lett.*, 7, 014007.

702 Dai, L., Che, T., Ding, Y., & Hao, X. (2017). Evaluation of snow cover and snow depth on the Qinghai–Tibetan
703 Plateau derived from passive microwave remote sensing. *Cryosphere*, 11, 1933-1948.

704 Dee, D.P., Uppala, S.M., Simmons, A.J., Berrisford, P., Poli, P., Kobayashi, S., Andrae, U., Balmaseda, M.A.,
705 Balsamo, G., Bauer, P., Bechtold, P., Beljaars, A.C.M., van de Berg, L., Bidlot, J., Bormann, N., Delsol, C.,
706 Dragani, R., Fuentes, M., Geer, A.J., Haimberger, L., Healy, S.B., Hersbach, H., Hólm, E.V., Isaksen, L.,
707 Kållberg, P., Köhler, M., Matricardi, M., McNally, A.P., Monge-Sanz, B.M., Morcrette, J.J., Park, B.K., Peubey,
708 C., de Rosnay, P., Tavolato, C., Thépaut, J.N., & Vitart, F. (2011). The ERA-Interim reanalysis: configuration
709 and performance of the data assimilation system. *Q. J. R. Meteorol. Soc.*, 137, 553-597.

710 Dong, J., Zhang, G., Zhang, Y., & Xiao, X. (2013). Reply to Wang et al.: Snow cover and air temperature affect the
711 rate of changes in spring phenology in the Tibetan Plateau. *Proc. Natl. Acad. Sci. U S A*, 110, E2856-E2857.

712 Franch, B., Vermote, E., Roger, J.-C., Murphy, E., Becker-Reshef, I., Justice, C., Claverie, M., Nagol, J., Csaszar, I.,

713 Meyer, D., Baret, F., Masuoka, E., Wolfe, R., & Devadiga, S. (2017). A 30+ Year AVHRR land surface
714 reflectance climate data record and its application to wheat yield monitoring. *Remote Sens.*, 9, 296

715 Frei, A., Tedesco, M., Lee, S., Foster, J., Hall, D.K., Kelly, R., & Robinson, D.A. (2012). A review of global
716 satellite-derived snow products. *Adv. Space Res.*, 50, 1007-1029. <https://doi.org/10.1016/j.asr.2011.12.021>.

717 Friedl, M.A., Sulla-Menashe, D., Tan, B., Schneider, A., Ramankutty, N., Sibley, A., & Huang, X. (2010). MODIS
718 Collection 5 global land cover: Algorithm refinements and characterization of new datasets. *Remote Sens.*
719 *Environ.*, 114, 168-182. <https://doi.org/10.1016/j.rse.2009.08.016>.

720 Gao, L., Hao, L., & Chen, X.-w. (2014). Evaluation of ERA-interim monthly temperature data over the Tibetan
721 Plateau. *J. Mt. Sci.*, 11, 1154-1168.

722 Hall, D.K., & Riggs, G.A. (2007). Accuracy assessment of the MODIS snow products. *Hydrol. Process.*, 21,
723 1534-1547

724 Hall, D.K., Riggs, G.A., & Salomonson, V.V. (1995). Development of methods for mapping global snow cover using
725 Moderate Resolution Imaging Spectroradiometer Data. *Remote Sens. Environ.*, 54, 127-140.
726 [https://doi.org/10.1016/0034-4257\(95\)00137-P](https://doi.org/10.1016/0034-4257(95)00137-P).

727 Hall, D.K., Riggs, G.A., Salomonson, V.V., DiGirolamo, N.E., & Bayr, K.J. (2002). MODIS snow-cover products.
728 *Remote Sens. Environ.*, 83, 181-194

729 Hansen, J., Ruedy, R., Sato, M., & Lo, K. (2010). Global surface temperature change. *Rev. Geophys.*, 48, RG4004

730 Helfrich, S.R., McNamara, D., Ramsay, B.H., Baldwin, T., & Kasheta, T. (2007). Enhancements to, and forthcoming
731 developments in the Interactive Multisensor Snow and Ice Mapping System (IMS). *Hydrol. Process.*, 21,

732 1576-1586

733 Hori, M., Sugiura, K., Kobayashi, K., Aoki, T., Tanikawa, T., Kuchiki, K., Niwano, M., & Enomoto, H. (2017). A
734 38-year (1978–2015) Northern Hemisphere daily snow cover extent product derived using consistent objective
735 criteria from satellite-borne optical sensors. *Remote Sens. Environ.*, 191, 402-418.
736 <https://doi.org/10.1016/j.rse.2017.01.023>.

737 Huang, X., Hao, X., Feng, Q., Wang, W., & Liang, T. (2014). A new MODIS daily cloud free snow cover mapping
738 algorithm on the Tibetan Plateau. *Sci. Cold Arid. Reg.*, 6, 0116–0123

739 Kang, S., Xu, Y., You, Q., Flügel, W.-A., Pepin, N., & Yao, T. (2010). Review of climate and cryospheric change in
740 the Tibetan Plateau. *Environ. Res. Lett.*, 5, 015101

741 Kelly, R.E., Chang, A.T., Tsang, L., & Foster, J.L. (2003). A prototype AMSR-E global snow area and snow depth
742 algorithm. *IEEE Trans. Geosci. Remote Sens.*, 41, 230-242

743 Key, J.R., Mahoney, R., Liu, Y., Romanov, P., Tschudi, M., Appel, I., Maslanik, J., Baldwin, D., Wang, X., & Meade,
744 P. (2013). Snow and ice products from Suomi NPP VIIRS. *Journal of Geophysical Research: Atmospheres*, 118,
745 12,816-812,830

746 Khlopenkov, K.V., & Trishchenko, A.P. (2007). SPARC: New cloud, snow, and cloud shadow detection scheme for
747 historical 1-km AVHRR data over Canada. *J. Atmospheric Ocean. Technol.*, 24, 322-343.
748 <https://doi.org/10.1175/JTECH1987.1>.

749 Kidder, S.Q. (1987). A multispectral study of the St. Louis area under snow-covered conditions using NOAA-7
750 AVHRR data. *Remote Sens. Environ.*, 22, 159-172. [https://doi.org/10.1016/0034-4257\(87\)90056-3](https://doi.org/10.1016/0034-4257(87)90056-3).

751 Larson, C. (2011). 'Third pole' glacier research gets a boost from China. *Science*, 334, 1199.

752 Ma, Y., Wang, Y., Wu, R., Hu, Z., Yang, K., Li, M., Ma, W., Zhong, L., Sun, F., Chen, X., Zhu, Z., Wang, S., & H., I.
753 (2009). Recent advances on the study of atmosphere-land interaction observations on the Tibetan Plateau.
754 *Hydrol. Earth Syst. Sci.*, 13, 1103-1111. <https://doi.org/10.5194/hess-13-1103-2009>.

755 Vermote E., Justice C., Csiszar I., Eidenshink J., Myneni R., Baret F., Masuoka E., Wolfe R., Claverie M. and
756 NOAA CDR Program (2014): NOAA Climate Data Record (CDR) of AVHRR Surface Reflectance, Version 4.
757 NOAA National Climatic Data Center. doi:10.7289/V5TM782M.

758 Polashenski, C.M., Dibb, J.E., Flanner, M.G., Chen, J.Y., Courville, Z.R., Lai, A.M., Schafer, J.J., Shafer, M.M., &
759 Bergin, M. (2015). Neither dust nor black carbon causing apparent albedo decline in Greenland's dry snow zone:
760 Implications for MODIS C5 surface reflectance. *Geophys. Res. Lett.*, 42, 9319-9327.

761 Pu, Z., Xu, L., & Salomonson, V.V. (2008). MODIS/Terra observed snow cover over the Tibet Plateau: distribution,
762 variation and possible connection with the East Asian Summer Monsoon (EASM). *Theor. Appl. Climatol.*, 97,
763 265-278

764 Pulliainen, J. (2010). Overview on GlobSnow Project: key questions to be resolved (coverage, aggregation,
765 validation, towards a future ECV), in: The 1st ESA DUE GlobSnow User Workshop, Innsbruck, Austria.

766 Qian, Y., Flanner, M.G., Leung, L.R., & Wang, W. (2011). Sensitivity studies on the impacts of Tibetan Plateau
767 snowpack pollution on the Asian hydrological cycle and monsoon climate. *Atmos. Chem. Phys.*, 11, 1929-1948.
768 <https://doi.org/10.5194/acp-11-1929-2011>.

769 Qu, X., & Hall, A. (2014). On the persistent spread in snow-albedo feedback. *Clim. Dyn.*, 42, 69–81

770 Riihelä, A., Manninen, T., Laine, V., Andersson, K., & Kaspar, F. (2013). CLARA-SAL: a global 28 yr timeseries of
771 Earth's black-sky surface albedo. *Atmos. Chem. Phys.*, 13, 3743-3762.
772 <https://doi.org/10.5194/acp-13-3743-2013>.

773 Robinson, D.A., Dewey, K.F., & Richard R. Heim, J. (1993). Global Snow Cover Monitoring: An Update. *Bull.*
774 *Amer. Meteor. Soc.*, 74, 1689-1696. [https://doi.org/10.1175/1520-0477\(1993\)074<1689:GSCMAU>2.0.CO;2](https://doi.org/10.1175/1520-0477(1993)074<1689:GSCMAU>2.0.CO;2).

775 Tsutsui, H., & Koike, T. (2012). Development of Snow Retrieval Algorithm Using AMSR-E for the BJ
776 Ground-Based Station on Seasonally Frozen Ground at Low Altitude on the Tibetan Plateau. *J. Meteor. Soc.*
777 *Japan*, 90, 99-112.

778 Wu, Z., Jiang, Z., Li, J., Zhong, S., & Wang, L. (2012). Possible association of the western Tibetan Plateau snow
779 cover with the decadal to interdecadal variations of northern China heatwave frequency. *Clim. Dyn.*, 39,
780 2393-2402.

781 Yao, T., Thompson, L., Yang, W., Yu, W., Gao, Y., Guo, X., Yang, X., Duan, K., Zhao, H., Xu, B., Pu, J., Lu, A.,
782 Xiang, Y., Kattel, D.B., & Joswiak, D. (2012). Different glacier status with atmospheric circulations in Tibetan
783 Plateau and surroundings. *Nat. Clim. Chang.*, 2, 663-667.

784 Yu, J., Zhang, G., Yao, T., Xie, H., Zhang, H., Ke, C., & Yao, R. (2016). Developing Daily Cloud-Free Snow
785 Composite Products From MODIS Terra–Aqua and IMS for the Tibetan Plateau. *IEEE Trans. Geosci. Remote*
786 *Sens.*, 54, 2171-2180.

787 Zhou, H., Aizen, E., & Aizen, V. (2013). Deriving long term snow cover extent dataset from AVHRR and MODIS
788 data: Central Asia case study. *Remote Sens. Environ.*, 136, 146-162. <https://doi.org/10.1016/j.rse.2013.04.015>.